



# 1 De-risking the energy transition by quantifying the uncertainties in fault stability

2 David Healy<sup>1</sup> & Stephen P. Hicks<sup>2</sup>

3 <sup>1</sup>School of Geosciences, University of Aberdeen, Aberdeen AB24 3UE United Kingdom

4 <sup>2</sup>Department of Earth Science and Engineering, Imperial College, London SW7 2AZ United Kingdom

5 [d.healy@abdn.ac.uk](mailto:d.healy@abdn.ac.uk)

6

## 7 Abstract

8 The operations needed to decarbonise our energy systems increasingly involve faulted rocks in the  
9 subsurface. To manage the technical challenges presented by these rocks and the justifiable public concern  
10 over induced seismicity, we need to assess the risks. Widely used measures for fault stability, including slip  
11 and dilation tendency and fracture susceptibility, can be combined with Response Surface Methodology from  
12 engineering and Monte Carlo simulations to produce statistically viable ensembles for the analysis of  
13 probability. In this paper, we describe the implementation of this approach using custom-built open source  
14 Python code (pfs – probability of fault slip). The technique is then illustrated using two synthetic datasets and  
15 two case studies drawn from active or potential sites for geothermal energy in the UK, and discussed in the  
16 light of induced seismicity focal mechanisms. The analysis of probability highlights key gaps in our knowledge  
17 of the stress field, fluid pressures and rock properties. Scope exists to develop, integrate and exploit citizen  
18 science projects to generate more and better data, and simultaneously include the public in the necessary  
19 discussions about hazard and risk.

20

## 21 Introduction

### 22 *Rationale & Objectives*

23 Faults in the crust slip in response to changes in stress or pore fluid pressure, and the source of these changes  
24 can be either natural or anthropogenic. Estimating the likelihood of slip on a particular fault for a given  
25 change in loading is critical for the industrial operations of the energy transition, especially geothermal  
26 energy and carbon sequestration and storage (CCS). The target formations of these operations are nearly  
27 always faulted and fractured to some degree, and experience from waste-water injection in the USA shows  
28 how even small changes in pore fluid pressure can trigger frequent seismic slip on these faults, with  
29 significant and widespread impact on society (e.g., Elsworth et al., 2016; Hincks et al., 2018; Hennings et al.,  
30 2019).

31 Stephenson et al. (2019) have shown how quantitative analysis of the subsurface is one of the key  
32 contributions that geoscientists can make to decarbonising energy production to meet national and  
33 international targets (e.g., CCC, 2019; IPCC, 2018). This includes the systematic geomechanical  
34 characterisation of rock formations, better understanding of fluid flow in fractured rocks, and the need for  
35 pilot projects to explore the scaling of behaviours from the laboratory to the field. Perhaps the most  
36 important aspect is to understand the public attitudes to subsurface decarbonisation technology  
37 (Stephenson et al., 2019; Roberts et al., 2021). Several recent studies have addressed the uncertainties in  
38 subsurface structural analysis of faulted rocks (Bond, 2015; Alcalde et al., 2017; Miocic et al., 2019). In this  
39 paper, we extend this work to specifically include fault stability, and argue that in order to simultaneously  
40 address public concerns and assess the viability of different schemes, we need a more rigorous approach to  
41 risking subsurface decarbonisation activities, especially where these involve changes in load on faulted rocks.

42 Useful measures of fault stability include slip and dilation tendency ( $T_s$  and  $T_d$  respectively) and fracture  
43 susceptibility ( $S_f$ , the change in fluid pressure to push effective stress to failure). These measures are defined  
44 as functions of the *in situ* stress, the orientation of the fault plane and, in the case of  $S_f$ , rock properties. It is  
45 widely recognised that the inputs for the prediction of stability are always uncertain, and to varying degrees:  
46 e.g., the vertical stress component of the *in situ* stress tensor can often be quite well constrained (to within



47 5%) from density log data, whereas the maximum horizontal stress is generally much harder to quantify. To  
48 improve and focus our predictions of fault stability in the subsurface, we need to accept and incorporate  
49 these uncertainties into our calculations. In this paper, we describe and explore a statistical approach to fault  
50 stability calculations, and then apply these methods to examples in geothermal energy, in both low- and  
51 high-enthalpy settings.

52 The specific aims of this paper are to:

- 53 1. describe and explain the Response Surface Methodology, and show how it can be applied to the  
54 probabilistic estimation of fault stability using a range of different measures;
- 55 2. explore how the main variables – in situ stress, fault orientation and rock properties – relate to the different  
56 measures of fault stability ( $T_s$ ,  $T_d$  and  $S_f$ ) using synthetic (i.e., artificial) data;
- 57 3. use case studies of active and proposed geothermal projects with publicly available data to illustrate the  
58 method, and then highlight the relationships between our known but uncertain input data and the predicted  
59 risk of fault slip.

#### 60 *Importance & Previous work*

61 Small changes in stress or fluid pressure (e.g., a few MPa) from human activities can have significant  
62 consequences for fault stability. For example, waste-water injection from hydraulic fracturing (“fracking”)  
63 operations has led to dramatic increases in seismicity in Oklahoma since 2009 (Hincks et al., 2018) and in  
64 Texas since 2008 (Hennings et al., 2019; Hicks et al., 2021). The precise mechanical cause(s) of this seismicity  
65 is the subject of some debate, and could be due to either ‘direct’ pore fluid pressure transfer to basement-  
66 hosted faults leading to a reduction in effective stress, or ‘indirect’ poroelastic effects at a distance (Elsworth  
67 et al., 2016; Goebel et al., 2019). The concept of critically stressed faults in the crust (Townend & Zoback,  
68 2000), where relatively high permeability serves to maintain near-hydrostatic pore pressures, is consistent  
69 with the idea that only minor perturbations in loading can have dramatic consequences, even in areas of  
70 apparently low seismicity and, implicitly, low background tectonic loading.

71 In densely populated areas such as the UK, public support for, and confidence in, subsurface operations are  
72 key. Hydraulic fracturing operations for shale gas in Lancashire (UK) were stopped after earthquakes were  
73 triggered by fluid injection (Clarke et al., 2019). Triggered felt seismicity has already been reported at the  
74 United Downs deep geothermal pilot in Cornwall (Holmgren & Werner, 2021). Note that, in both of these  
75 cases, fracturing and/or fault slip are intrinsic to the success of the operation as they are needed to enhance  
76 fluid flow, and therefore earthquakes are inevitable. In detail, microseismicity (i.e.,  $M < 2$ ) is inevitable, but it  
77 is important to understand whether felt (i.e.  $M > 2$ ) seismicity can be forecast ahead of time. Furthermore,  
78 many sites for energy transition projects in the UK are located in (beneath) areas of extreme poverty and  
79 social deprivation, both rural (e.g., Cornwall, South Wales) and urban (e.g., Greater Manchester, Glasgow),  
80 and therefore the risks from these projects fall disproportionately on the less well off (Nolan, 2016;  
81 McLennan et al., 2019). To begin to address these complex issues, we need to quantify which faults are more  
82 or less likely to slip in response to induced changes in loading. One approach is to analyse data during  
83 subsurface operations and attempt to manage the consequences (e.g., Verdon & Budge, 2018). An  
84 alternative approach, and the one taken in this paper, is to look at the bigger picture before operations  
85 commence and reduce risk from the outset.

86 Various measures have been proposed to quantify the propensity or tendency of a given fault to slip (or  
87 open) in a known stress field. The following methods are based around an assumption of Mohr-Coulomb  
88 (brittle-plastic) failure which has been shown to capture the key aspects of faulting in the upper crust. Slip  
89 tendency ( $T_s$ ) was introduced by Morris et al. (1996) and is the simplest measure of fault stability, defined as:

$$90 \quad T_s = \tau / \sigma_n \quad (1)$$

91 where  $\tau$  is the shear stress and  $\sigma_n$  is the normal stress acting on the fault plane. These stress components in  
92 turn depend on the principal stresses and the orientation of the fault plane (see Lisle & Srivastava, 2004 for  
93 details). In the absence of cohesion, if the slip tendency on a fault equals or exceeds the coefficient of sliding  
94 friction, then the fault can be deemed “unstable”. This dimensionless index embodies the key mechanical



95 principle underlying Mohr-Coulomb shear failure: as the shear (“sliding”) stress acting on a fault plane rises  
 96 in relation to the normal (or “clamping”) stress, the fault approaches failure and will slip. Dilation tendency  
 97 ( $T_d$ ) has been defined to describe the propensity for a fault to open, or dilate, in a given stress regime:

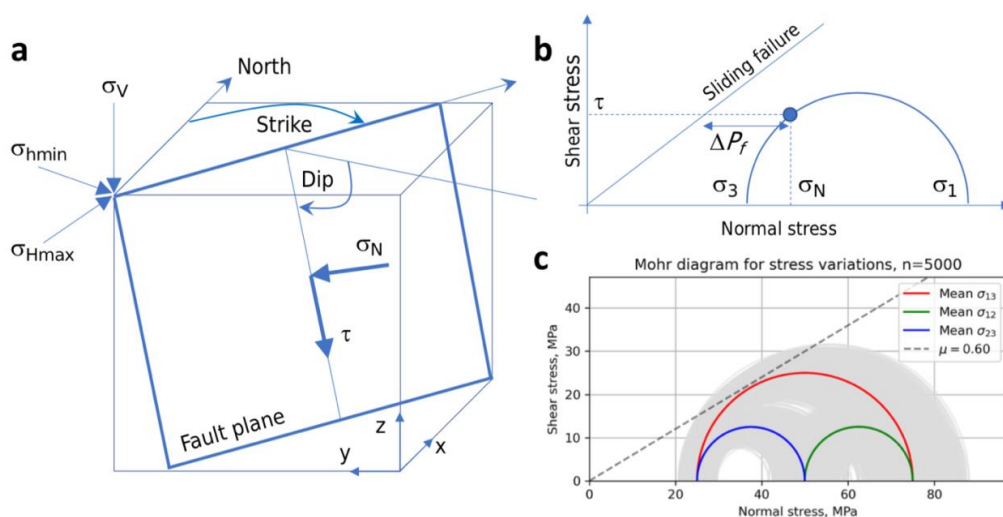
$$98 \quad T_d = (\sigma_1 - \sigma_n) / (\sigma_1 - \sigma_3) \quad (2)$$

99 where  $\sigma_1$  and  $\sigma_3$  are the principal stresses of the *in situ* stress tensor (Ferrill et al., 1999).

100 Most rocks in the upper crust are porous and permeable to some degree, and fault rocks are no exception,  
 101 so these rocks are generally fluid saturated. This implies that we should include pore fluid pressure and the  
 102 concept of effective stress in our assessment of fault stability. Fracture susceptibility ( $S_f$ ) is the change in pore  
 103 fluid pressure needed to push a stressed fault to failure (Streit & Hillis, 2004) and is defined by:

$$104 \quad S_f = \Delta P_f = (\sigma_n - P_f) - (\tau - C_0) / \mu \quad (3)$$

105 where  $P_f$  is the pore fluid pressure at the fault,  $C_0$  is the cohesive strength (or cohesion), and  $\mu$  is the  
 106 coefficient of sliding friction (see Figure 1b).



107  
 108 **Figure 1. a.** Schematic block diagram of a fault plane showing the terminology used in this paper. Also shown  
 109 are the cartesian and geographic reference frames and the Andersonian principal stresses. **b.** Mohr diagram  
 110 for a given state of stress (blue semi-circle) with normal ( $\sigma_n$ ) and shear stresses ( $\tau$ ) marked for a selected fault  
 111 plane orientation (blue dot). Failure envelope for frictional sliding (cohesion=0) also shown as straight blue  
 112 line. **c.** Mohr diagram depicting one of the key issues tackled in this paper: given uncertainty in the input  
 113 stress values (grey Mohr circles for the variation around the average principal stresses in red, blue and green),  
 114 what is the probability of failure? i.e., what percentage of all these stress states will intersect the failure  
 115 envelope?

116 Previous applications of these three measures of fault stability –  $T_s$ ,  $T_d$  and  $S_f$  – cover the full spectrum of rock  
 117 types and stress fields, from basins to basement and from extensional, contractional and wrench tectonic  
 118 settings. Applications within the domain of the energy transition include examples from geothermal energy  
 119 (both shallow and deep) and CCS. The original definition of fracture susceptibility by Streit & Hillis (2004) was  
 120 concerned with safe injection limits for CO<sub>2</sub> in potential reservoirs in Australia. Moeck et al. (2009) used slip  
 121 tendency to quantify the relative stability of different fault sets in different horizons in a geothermal reservoir  
 122 in the North German Basin, and Barcelona et al. (2019) used a similar method for Copahue geothermal  
 123 reservoir in Argentina. For CCS, Williams et al., (2016, 2018) have used slip tendency analyses of faults in  
 124 potential sandstone reservoirs on the UK continental shelf, including the North Sea and East Irish Sea basins.  
 125 The links between subsurface fluid flow, seismicity, and fault stability have recently been explored by Das &



126 Mallik (2020) for the Koyana earthquakes in India, and by Wang et al. (2020) for strike-slip faults in the Tarim  
 127 Basin of China.

128 Probabilistic approaches to fault stability have been adopted by various workers. In risking CO<sub>2</sub> storage for  
 129 an oil reservoir in the Williston basin, Ayash et al. (2009) used a features, events and processes (FEP)  
 130 approach to constrain the likelihood of occurrence of fault slip (based on slip tendency) and the severity of  
 131 the consequences, with their product defined as the risk. Rohmer & Bouc (2010) used RSM to assess cap rock  
 132 integrity for tensile or shear failure above deep aquifers in the Paris basin targeted for the storage of CO<sub>2</sub>.  
 133 Coupled RSM and Monte Carlo approaches to fault stability have been used by Chiaramonte et al. (2008) and  
 134 Walsh & Zoback (2016), following their initial application in the field of wellbore stability by Moos et al.  
 135 (2003). This Fault Slip Potential (FSP) method developed by Stanford (e.g., Chiaramonte et al., 2008 & Walsh  
 136 & Zoback, 2016) calculates the response surface for fracture susceptibility, with the in situ stress tensor  
 137 calculated by inversion of abundant seismicity data (focal mechanisms), and then uses a Monte Carlo  
 138 simulation to generate cumulative distribution functions (CDFs) of conditional probability of slip defined with  
 139 reference to an arbitrary pore pressure perturbation ( $\Delta P_f = 2$  MPa, in the case of Walsh & Zoback, 2016).  
 140 Note that FSP assumes cohesionless faults ( $C_0=0$ ) and hydrostatic pore fluid pressure, and that *conditional*  
 141 probability in this sense refers to the fact that we do not know where any particular fault is with respect to  
 142 the seismic cycle.

143 *Conventions and layout for this paper*

144 In the sections below, we describe the underlying equations for measuring fault stability and then show how  
 145 we can use Response Surface Methodology (RSM) from engineering to explore the consequences of  
 146 uncertainties in the input variables. After assessing the quality of the solutions obtained from RSM, we then  
 147 apply a brute force Monte Carlo (MC) approach to generate cumulative distribution functions (CDFs) of the  
 148 different measures ( $T_s$ ,  $T_d$  and  $S_f$ ). The case studies use published, publicly available data to constrain the  
 149 input variable distributions and then a combined RSM/MC approach is used to explore the uncertainty in  
 150 fault stability in different settings.

151 In this paper, compressive stress is reckoned positive, with  $\sigma_1$  as the maximum compressive principal stress  
 152 and  $\sigma_3$  as the minimum principal stress. Stress states and fault regimes are assumed to be Andersonian, with  
 153 one principal stress vertical, although the underlying model and code could be changed to incorporate non-  
 154 Andersonian stress states with the addition of extra variables for the stress tensor orientation (Walsh &  
 155 Zoback, 2016). The likelihood of slip on a fault is assessed in the framework of Mohr-Coulomb failure, with  
 156 or without cohesion (Jaeger et al., 2009). Fault orientations are quantified as strike and dip, following the  
 157 right-hand rule: with your right hand flat on the fault plane and fingers pointing down dip, the right thumb  
 158 points in the direction (azimuth) of strike. The relationship between the geographical and cartesian reference  
 159 frames follows a North-East-Down convention. Figure 1 depicts the key terms and elements used in the  
 160 analysis, and Table 1 contains a list of terms and symbols used with units where appropriate.

Quantity	Symbol	Units
Maximum compressive stress	$\sigma_1$	MPa
Intermediate compressive stress	$\sigma_2$	MPa
Minimum compressive stress	$\sigma_3$	MPa
Vertical stress	$\sigma_v$	MPa
Maximum horizontal stress	$\sigma_{Hmax}$	MPa
Minimum horizontal stress	$\sigma_{Hmin}$	MPa
Azimuth of max. horizontal stress	$\phi_{HAZ}$	°
Pore fluid pressure	$P_f$	MPa
Coefficient of friction	$\mu$	dimensionless
Cohesive strength (or cohesion)	$C_0$	MPa
Slip tendency	$T_s$	dimensionless
Dilation tendency	$T_d$	dimensionless
Fracture susceptibility	$S_f$	MPa
Fault strike	$\varphi$	°



Fault dip	$\delta$	°
Shear stress on a fault plane	$\tau$	MPa
Normal stress on a fault plane	$\sigma_n$	MPa

161

162 **Table 1.** List of terms and symbols used in this paper, with units where appropriate.

163

164 **Statistical analysis of geomechanical fault stability**

165 *Introduction to Response Surface Methodology (RSM)*

166 RSM is widely used in engineering and industry along with a Design of Experiments approach, and often  
 167 employed to optimise a specific process of interest – e.g., to maximise the yield of a reaction given the input  
 168 variables of pressure, temperature, reactant mass etc. RSM is a large and growing field and is best considered  
 169 as a toolbox of different methods with a common mathematical basis. The governing equations for RSM were  
 170 derived by Box & Wilson (1951). The core idea is that a response  $y$  can be represented by a polynomial  
 171 function of a number ( $q$ ) of input variables  $x_1 - x_q$ :

172 
$$y = f(x_1, x_2, \dots, x_q) \quad (4)$$

173 Each of the  $q$  input variables can be represented by either a discrete set of measurements made in the  
 174 laboratory (or field) or drawn from appropriate statistical distributions (normal/Gaussian, skewed normal,  
 175 Von Mises etc.). The simplest polynomial function that relates  $y$  and  $x$  is a linear one:

176 
$$y_i = \beta_0 + \beta_1 x_{i1} + \beta_2 x_{i2} + \dots + \beta_q x_{iq} + \epsilon_i \quad (5)$$

177 
$$y_i = \beta_0 + \sum_{j=1}^q \beta_j x_{ij} + \epsilon_i \quad (6)$$

178 where  $\beta_q$  are the coefficients (to be determined),  $y_i$  is the set of observations of the response ( $i = 1, 2, \dots, N$ ),  
 179 and  $x_{ij}$  are the input variables ( $j = 1, 2, \dots, q$ ).  $\epsilon$  is the experimental error, and the number of ‘observations’  $N$   
 180  $> q$ , the number of input variables. This is therefore a multiple regression model linking the response  $y$  to  
 181 more than one (i.e., multiple) independent variables,  $x$ .

182 A more complex polynomial relationship is the quadratic form:

183 
$$y = \beta_0 + \sum_{j=1}^q \beta_j x_j + \sum_{j=1}^q \beta_{jj} x_j^2 + \sum_{i < j} \beta_{ij} x_i x_j + \epsilon \quad (7)$$

184 This 2<sup>nd</sup> order multiple regression model contains all the terms of the linear (1<sup>st</sup> order) model, but also extra  
 185 terms for the squares and cross-products of the input variables (second and third terms on the RHS of  
 186 equation 7).

187 To define a response surface, either linear or quadratic, we need to calculate the values of the  $\beta_q$  coefficients.  
 188 We can rewrite the key equations in matrix form:

189 
$$\mathbf{y} = \mathbf{X}\boldsymbol{\beta} + \boldsymbol{\epsilon} \quad (8)$$

190 where  $\mathbf{y}$  is an ( $N \times 1$ ) vector of observations (or calculations),  $\mathbf{X}$  is an ( $N \times k$ ) matrix of input variable values ( $k$   
 191  $= q + 1$ ), and  $\boldsymbol{\beta}$  is a ( $k \times 1$ ) vector of regression coefficients. We solve this system of equations using the  
 192 standard linear algebra technique of least squares regression (Myers et al., 2016):

193 
$$\hat{\boldsymbol{\beta}} = (\mathbf{X}'\mathbf{X})^{-1}\mathbf{X}'\mathbf{y} \quad (9)$$

194 The response surface (linear or quadratic) is then defined by

195 
$$\hat{y} = \mathbf{X}\hat{\boldsymbol{\beta}} \quad (10)$$

196 The values used in  $\mathbf{X}$  are chosen to efficiently span the parameter space. A typical sampling design for  $\mathbf{X}$  is  
 197 called the 3<sup>q</sup> model with 3 values of each variable, usually the minimum, mean (or mode) and maximum. For  
 198 slip tendency,  $q = 6$  and this means we use  $3^q = 3^6 = 729$  data points to calculate the response surface. In



199 practice, coded variables are used in  $\mathbf{X}$  where the absolute values for the minimum, mean and maximum of  
200 each variable are scaled to  $-1$ ,  $0$  and  $+1$  respectively, and then scaled back when the response surface is used  
201 in the Monte Carlo simulation (Myers et al., 2016).

202 The response surface – i.e., the set of  $\beta$  coefficients – is defined using a limited number of sample points,  
203 depending on the chosen sample design ( $3^q$  in the examples used in this paper; other variants exist – see  
204 Myers et al., 2016 for details). To explore the possible variations of a response more fully, we use a Monte  
205 Carlo (MC) approach of pre-defined size ( $N_{MC} = 5,000$  in the examples in this paper). The MC simulation uses  
206 the response surface calculated from the design points to calculate the responses for  $N_{MC}$  combinations of  
207 input variables drawn from their distributions. This produces a statistically viable ensemble of response  
208 values from which we can infer the probability of the response with respect to a chosen threshold.

209 With respect to fault stability, we can use RSM to produce a parameterised relationship – the response  
210 surface in  $q$  dimensions – between a stability measure of interest and the  $q$  input variables. In the case of slip  
211 tendency  $T_s$ , we can rewrite the components of equation 1 in terms of the measurable input quantities as  
212 follows:

$$213 \quad \tau = \sqrt{(\sigma_1 - \sigma_2)^2 l^2 m^2 + (\sigma_2 - \sigma_3)^2 m^2 n^2 + (\sigma_3 - \sigma_1)^2 l^2 n^2} \quad (11)$$

$$214 \quad \sigma_n = \sigma_1 l^2 + \sigma_2 m^2 + \sigma_3 n^2 \quad (12)$$

215 where  $l$ ,  $m$  and  $n$  are the direction cosines of the normal (pole) to the fault plane given by

$$216 \quad l = \sin \delta \sin \phi \quad (13a)$$

$$217 \quad m = -\sin \delta \cos \phi \quad (13b)$$

$$218 \quad n = \cos \delta \quad (13c)$$

219 where  $\phi$  is the fault strike and  $\delta$  is the fault dip, in a North-East-Down reference frame (Allmendinger et al.,  
220 2012).

221 All terms on the right-hand sides of equations 11-13 are uncertain to some degree, therefore estimating the  
222 uncertainty of  $T_s$ , and as importantly, the *key controls on the uncertainty of  $T_s$* , in terms of these input  
223 variables, is non-trivial. This difficulty in estimating and visualising possible variations in our estimates of  $T_s$   
224 is exacerbated by the recognition that each of the input variables may be distributed differently: some  
225 quantities (e.g., the principal stresses) may follow normal (Gaussian) statistics, whereas others (e.g., strike,  
226 dip, sHmax azimuth) will follow Von Mises distributions. In the case of fracture susceptibility ( $S_f$ , equation 3),  
227 it is even more complicated with the addition of three further input variables for friction, cohesion and pore  
228 fluid pressure. Measurements or calculations of coefficients of friction and cohesive strength often display  
229 asymmetric or skewed distributions (skewed high or low), and this adds further complexity to the task of  
230 estimating and constraining fault stability from the data at hand.

### 231 *Worked Example 1: Slip tendency from synthetic input data*

232 The calculations presented in this paper were all performed with the custom pfs (**p**robability of **f**ault **s**lip)  
233 package, written by the first author (DH) in Python 3, and freely available on GitHub (see Code Availability,  
234 below).

235 The first example calculates a response surface for slip tendency ( $T_s$ ) from  $q=6$  input variables: the  
236 magnitudes of the three principal stresses of the *in situ* stress tensor ( $\sigma_1, \sigma_2, \sigma_3$ ) assumed Andersonian with  
237 one principal stress vertical, the azimuth of the maximum horizontal stress (*sHaz*), and the strike and dip of  
238 the fault plane. This response surface is then used in a Monte Carlo simulation ( $N_{MC} = 5,000$ ) to generate a  
239 CDF of  $T_s$  values for the fault. The specific Python code to run this example in the pfs package is wrapped in  
240 a Jupyter notebook available on GitHub (WorkedExample1.ipynb).

241 The first task is to define the distributions of the input variables. In pfs, examples are shown for normal,  
242 skewed normal and Von Mises (circular normal) distributions, but other statistical distributions are allowed.  
243 Table 2 and Figure 2 describe the ranges and moments of these distributions for each input variable. For this



244 example, the normally distributed principal stresses are defined with a variation (standard deviation) of 5%  
 245 of their central (mean) value, and the Von Mises distributions of the azimuthal variables (sHaz, strike and dip)  
 246 all have  $\kappa = 200$  to model their dispersion about their mean. The fault of interest strikes  $060^\circ$  and dips  $60^\circ$  to  
 247 the south (right hand rule). The key questions to be addressed by this example are:

- 248 1. given these uncertainties in the input stresses and orientation data, how does the estimation of  $T_s$   
 249 vary? What is the range and the mode?
- 250 2. which variables exert the greatest (and least) control on the predicted variation in  $T_s$ ?

251 We first build a response surface using a  $3^q$  design, i.e., 3 data points for each variable – minimum, mean and  
 252 maximum – and for  $T_s$ ,  $q = 6$ . This means we calculate the response surface from  $3^6 = 729$  data points. We  
 253 compare a calculated linear response surface with a quadratic response surface, using a normal probability  
 254 plot of residuals (Figure 3). These residuals are the differences between the values of  $T_s$  derived from the  
 255 observations (taken from the input distributions shown in Table 2 (upper) and Figure 2), and the calculated  
 256 values of  $T_s$  using the  $\beta$  coefficients derived by least squares regression i.e., the response surface. The  
 257 adjusted  $R^2$  value for the quadratic 2<sup>nd</sup> order model is significantly better than that for a linear 1<sup>st</sup> order model,  
 258 and we use quadratic models throughout the rest of this paper. More detailed inspection of the quality of fit  
 259 between the response surface and the observations is possible, including analysis of variance, main effects  
 260 plots and the use of t-statistics for each input variable to quantify their significance to the definition of the  $\beta$   
 261 coefficients (Myers et al., 2016). In practice, visualising sections of the response surface for individual  
 262 variables is generally sufficient (see below; Moos et al., 2003; Walsh & Zoback, 2016).

Variable	Mean	Standard deviation ( $\kappa$ for Von Mises)	Units	Distribution	Comments
<b>Worked Example 1 – Synthetic <math>T_s</math> – modelled depth=3 km</b>					
$\sigma_v$ , vertical stress	75.0	3.75 (5% of mean)	MPa	Normal	Lithostatic for depth of 3 km, assuming average rock density of $2500 \text{ kg m}^{-3}$
$\sigma_H$ , max. horizontal stress	50.0	2.5 (5% of mean)	MPa	Normal	Andersonian normal faulting regime
$\sigma_h$ , min. horizontal stress	25.0	1.25 (5% of mean)	MPa	Normal	
Azimuth of $\sigma_{Hmax}$	060	$\kappa=200$	$^\circ$	Von Mises (circular Normal)	
Fault strike	060	$\kappa=200$	$^\circ$	Von Mises (circular Normal)	
Fault dip	60.0	$\kappa=200$	$^\circ$	Von Mises (circular Normal), truncated at 0 and 90	
<b>Worked Example 2 – Synthetic <math>S_f</math> – modelled depth=3 km</b>					
$\sigma_v$ , vertical stress	75.0	7.5 (10% of mean)	MPa	Normal	Lithostatic for depth of 3 km, assuming average rock density of $2500 \text{ kg m}^{-3}$
$\sigma_H$ , max. horizontal stress	55.0	5.5 (10% of mean)	MPa	Normal	
$\sigma_h$ , min. horizontal stress	35.0	3.5 (10% of mean)	MPa	Normal	

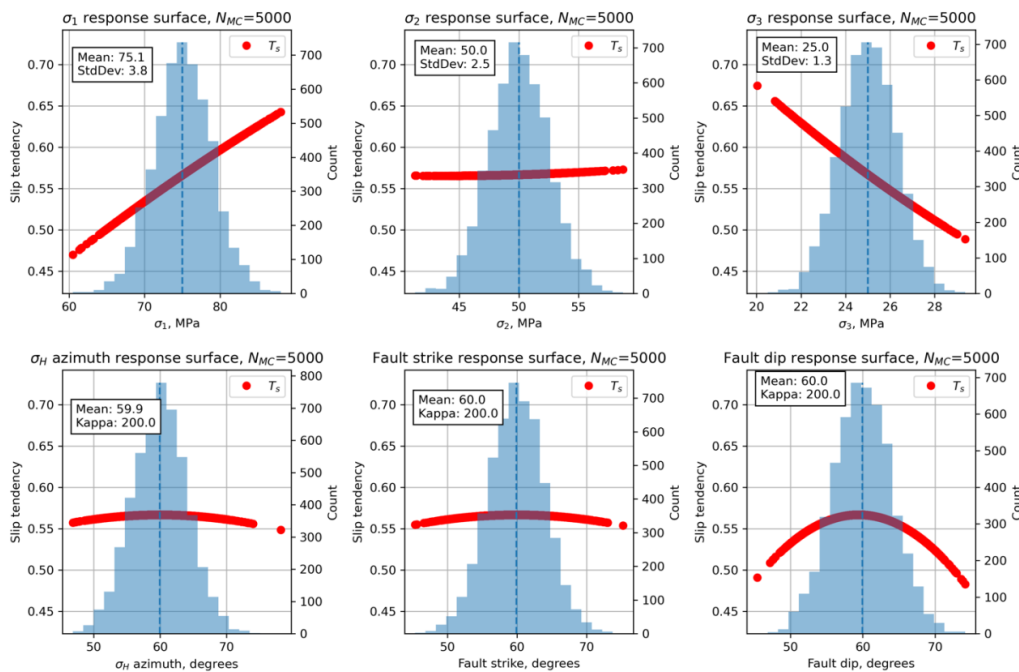




$P_f$ , pore fluid pressure	30.0	3.0 (10% of mean)	MPa	Normal	Hydrostatic for depth of 3 km, assuming fluid density=1000 kg m <sup>-3</sup>
Azimuth of $\sigma_{Hmax}$	060	$\kappa=200$	°	Von Mises (circular Normal)	
Fault strike	060	$\kappa=200$	°	Von Mises (circular Normal)	
Fault dip	60.0	$\kappa=200$	°	Von Mises (circular Normal), truncated at 0 and 90	
Friction, $\mu$	0.6	0.12 (20% of mean)	n/a	Skewed normal	$\alpha = -3$ i.e., skewed low
Cohesion, $C_0$	20.0	2.0 (10% of mean)	MPa	Skewed normal	$\alpha = +3$ i.e., skewed high

263

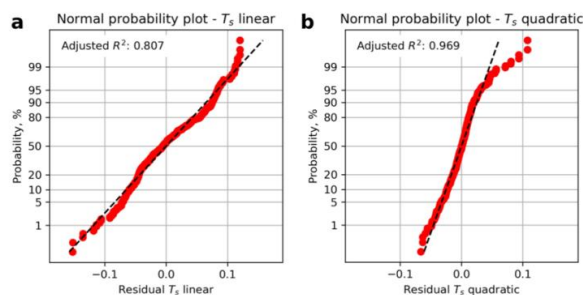
264 **Table 2.** Table of input variable distributions for the synthetic models in Worked Examples 1 and 2.



265

266 **Figure 2.** Histograms of input variables used to calculate slip tendency  $T_s$  for the synthetic distributions shown  
 267 in Table 2.





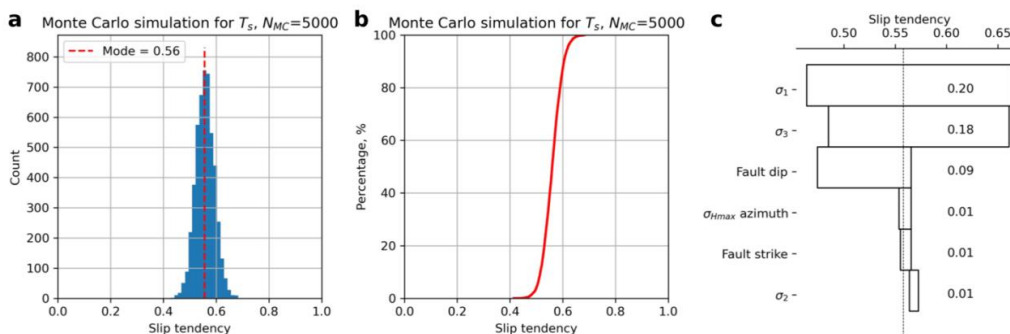
268

269 **Figure 3.** Residual plots for linear and quadratic response surfaces for slip tendency using synthetic data. The  
 270 quadratic fit has a higher value of the adjusted  $R^2$  parameter and is therefore deemed better in this case.

271 Having generated the quadratic response surface for  $T_s$  for these input distributions, we can now use it to  
 272 perform a Monte Carlo (MC) simulation with the aim of generating a statistically viable ensemble from which  
 273 we can infer the probability of  $T_s$  exceeding a critical value of sliding friction. The results from the MC analysis  
 274 of  $T_s$  are shown in Figure 4. The histogram of all values of  $T_s$  shows a symmetrical and rather narrow  
 275 distribution with a modal value of about 0.56 (Figure 4a). The CDF of all values of  $T_s$  also shows this narrow  
 276 and symmetrical distribution (Figure 4b).

277 A response surface of more than two variables is not easy to visualise. One approach is to take sections  
 278 through the surface at specific values of all but one variable and graph that. The red lines shown in Figure 2  
 279 depict the response surface for that variable with all other variables held at their mean values. Thus the red  
 280 line in Figure 2a shows the variation in  $T_s$  as  $\sigma_1$  varies with all other variables ( $\sigma_2$ ,  $\sigma_3$ ,  $sHaz$ ,  $\varphi$  and  $\delta$ ) held at  
 281 their mean values. There is a clear positive correlation of increasing  $T_s$  with increasing  $\sigma_1$ , as expected from  
 282 the definition of  $T_s$  and its underlying dependence on differential stress ( $=\sigma_1 - \sigma_3$ ); the clear negative  
 283 correlation of  $T_s$  with  $\sigma_3$  shown in Figure 2c confirms this. Many of the response surface sections shown in  
 284 Figure 2 are quasi-linear, but some are not: in particular, the dependencies of  $T_s$  on  $sHaz$ , strike and dip are  
 285 all non-linear, and this further justifies the selection of a 2<sup>nd</sup> order quadratic response surface model.

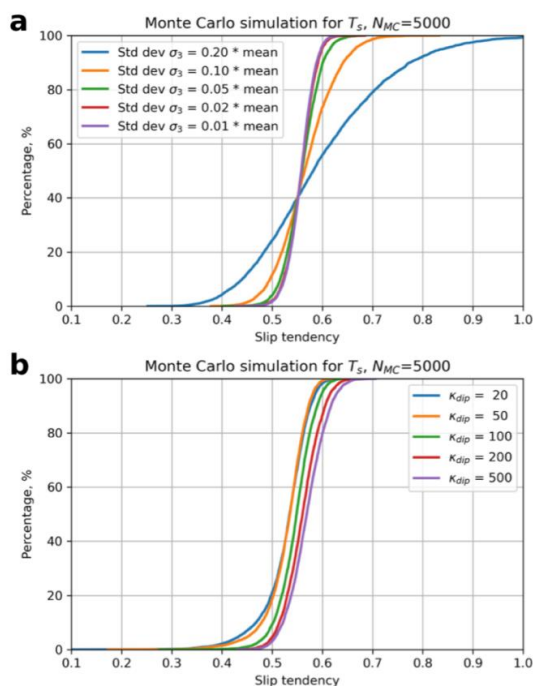
286 A useful way to visualise the results from the response surface calculated by the MC simulation is the tornado  
 287 plot shown in Figure 4c. Here the ranges of  $T_s$  for each input variable (shown as red lines over the histograms  
 288 in Figure 2) are plotted to show the relative sensitivity of  $T_s$  to each variable. Variables are ranked from the  
 289 largest range at the top to the lowest range at the bottom. Again, the core dependence of  $T_s$  on differential  
 290 stress ( $=\sigma_1 - \sigma_3$ ) is apparent, with  $\sigma_1$  and  $\sigma_3$  ranked highest in the plot. Interestingly, fault dip is ranked the  
 291 next highest in terms of sensitivity and this reflects the geometry of this particular example. The Andersonian  
 292 stress regime is for normal faulting, with  $\sigma_1$  vertical.  $\sigma_2$  is oriented parallel to fault strike ( $sHaz = strike = 060$ ),  
 293 and the fault dips at 60. This fault is therefore ideally oriented for slip in this stress field. Small changes to dip  
 294 will influence the ratio of  $\tau$  to  $\sigma_n$ , and therefore  $T_s$ .



295



296 **Figure 4.** Output from Monte Carlo simulation ( $N_{MC}=5,000$ ) of slip tendency calculated using a quadratic  
297 response surface from synthetic input data. **a.** Histogram of calculated slip tendency values, in this case  
298 showing a quasi-normal distribution with a mode of  $\sim 0.55$ . **b.** Cumulative distribution function (CDF) of  
299 calculated slip tendency values, showing the range in values from  $\sim 0.4$  to  $\sim 0.7$ . **c.** Tornado plot showing  
300 relative sensitivity to the input variables. The vertical dashed line shows the modal (most frequent) value of  
301  $T_s$  from the MC ensemble.



302

303 **Figure 5.** Output from Monte Carlo sensitivity tests for slip tendency,  $T_s$ . **a.** Effect of variation in standard  
304 deviation of the least principal stress,  $\sigma_3$ . **b.** Effect of variation in dispersion ( $\kappa$  parameter of the Von Mises  
305 distribution) of fault dip.

306 We can use a Monte Carlo approach to explore these sensitivities in more detail. Given the shape of the  
307 response surface sections shown in Figure 2 and the ranking of variables in Figure 4c, we can quantify how  
308 more or less variation in the inputs will affect the predicted  $T_s$ . Figure 5 shows the results of this sensitivity  
309 analysis for  $\sigma_3$  and fault dip. The most significant effect on the CDF of  $T_s$  is produced by increasing the  
310 variation in  $\sigma_3$  to 20% of the mean. This level of uncertainty for the minimum stress is not unreasonable in  
311 real-world scenarios (see Case Studies below). Increased uncertainty in  $\sigma_3$  at this level leads to a  $\sim 20\%$  chance  
312 of  $T_s$  being in excess of 0.7 ( $p = 0.8$  for  $T_s \leq 0.7$  from Figure 5a). Increased uncertainty in fault dip is achieved  
313 by varying the dispersion parameter  $\kappa$  of the Von Mises distribution (lower values of  $\kappa =$  more dispersed).  
314 Very disperse distributions of fault dip with  $\kappa = 20$  only change  $T_s$  by  $< 0.1$ .

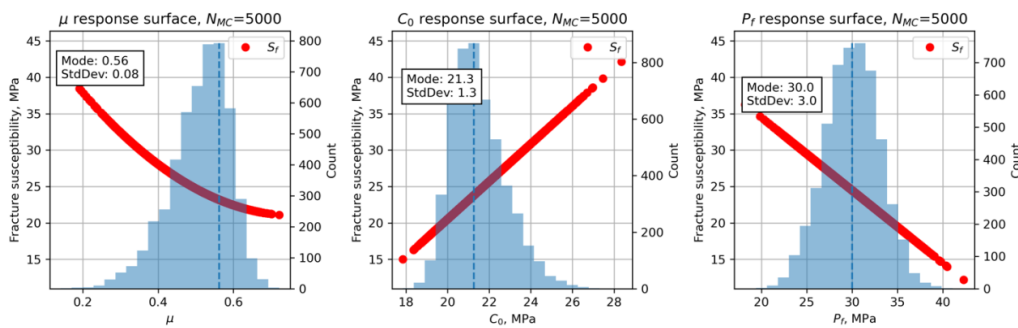
315 *Worked Example 2: synthetic Sf*

316 We can explore variations in predicted fracture susceptibility using the same principles as for slip tendency,  
317 but adjusted by incorporating three new variables as required by equation 3 – pore fluid pressure, friction  
318 coefficient and cohesion (code in GitHub: WorkedExample2.ipynb). The number of variables  $q$  is now 9, and  
319 therefore the design space used to compute the response surface is  $3^9 = 3^9 = 19,683$  data points. In practice  
320 this means a slower run-time, but still only takes a few minutes on a modern processor.

321 For this example, we use the same stress tensor as for the  $T_s$  example, with  $\sigma_1$  as the maximum principal  
322 stress and vertical, i.e., an Andersonian normal fault regime for a depth of approximately 3 km. We constrain

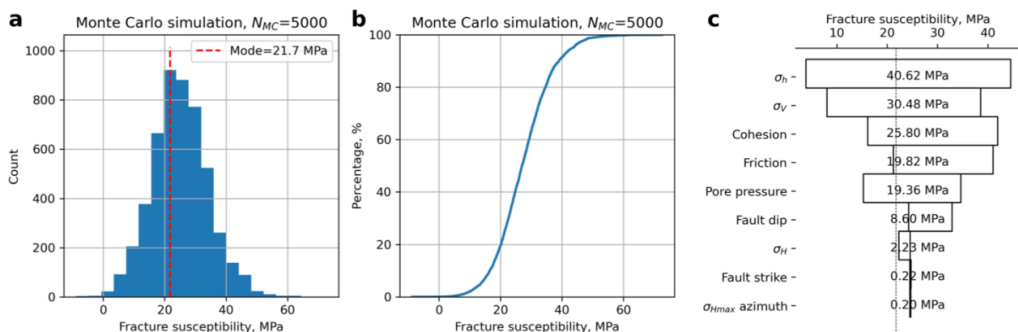


323 the *in situ* pore pressure with a symmetrical normal distribution with a mean value of 30 MPa, which is  
 324 approximately hydrostatic for a depth of 3 km, and with a variation of 10% of this mean. Friction is  
 325 constrained by a skewed normal distribution with a mode of 0.56 and  $\alpha = -3$ , i.e., skewed towards lower  
 326 values. This shape of distribution for friction coefficients is consistent with previous studies (e.g., Moos et al.,  
 327 2003; Walsh & Zoback, 2016) but is open to question (see Discussion). Similarly for cohesion, we use a skewed  
 328 normal distribution with a mode of 21 MPa and  $\alpha = +3$ , i.e., skewed towards higher values again consistent  
 329 with previous work. These input variable distributions are documented in Table 2 (lower) and shown in the  
 330 histograms of Figure 6.



331

332 **Figure 6.** Histograms of the input variables, in addition to those shown in Figure 2, used to calculate fracture  
 333 susceptibility for the synthetic distributions shown in Table 2. Note the skewed (asymmetric) distributions  
 334 for  $\mu$  and  $C_0$ .



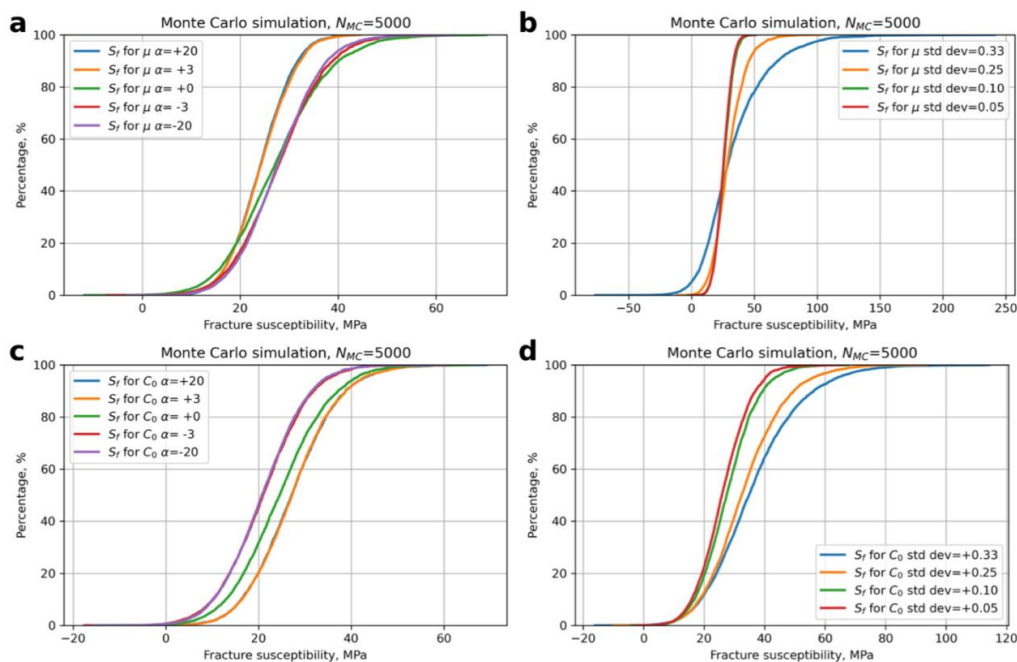
335

336 **Figure 7.** Output from Monte Carlo simulation ( $N_{MC}=5,000$ ) of fracture susceptibility calculated using a  
 337 quadratic response surface from synthetic input data. **a.** Histogram of calculated fracture susceptibility,  
 338 showing a quasi-normal distribution with a mode of 21.7 MPa. **b.** Cumulative distribution function (CDF) of  
 339 calculated fracture susceptibility, showing the range in values from just less than 0 to about 60 MPa. **c.**  
 340 Tornado plot of relative sensitivities of the input variables used to calculate fracture susceptibility.

341 We calculate a quadratic response surface and use a Monte Carlo simulation ( $N_{MC} = 5,000$ ) to generate the  
 342 ensemble summarised in Figure 7. The mode of the distribution of  $S_f$  is 21.7 MPa meaning that, on average,  
 343 an increase in pore fluid pressure of about 22 MPa above the average *in situ* value of 30 MPa is needed to  
 344 push the effective stress state to Mohr-Coulomb failure. The histogram in Figure 7a is approximately  
 345 symmetrical, perhaps with a slight skewness to higher values, and this is reflected in the CDF shown in Figure  
 346 7b. The distribution is overwhelmingly positive, meaning that this fault is almost unconditionally stable for  
 347 any change in pore fluid pressure, *at these conditions*. The response surface sections for  $\mu$ ,  $C_0$  and  $P_f$  shown  
 348 in Figure 6 (red lines) all show a strong influence on the fracture susceptibility, and these are confirmed in  
 349 the tornado plot of Figure 7c. Pore fluid pressure exhibits a negative correlation with  $S_f$  (Figure 6c) which is  
 350 consistent with the general principle of effective stress: i.e., if the original *in situ* pore pressure is already



351 high, it only takes a small perturbation (small  $\Delta P_f = S_f$ ) to promote sliding failure. The response to changes in  
352  $\mu$  and  $C_0$  is more interesting (Figure 6a and b). For this magnitude of cohesion, the effect of cohesion on  $S_f$  is  
353 greater than that of  $\mu$  ( $C_0$  ranks higher than  $\mu$  in the tornado plot, Figure 7c), and the dependence of  $S_f$  on  $\mu$   
354 is negative. However, this relationship is not general as will be shown in the Case Study for the Porthtowan  
355 Fault Zone (see below).



356

357 **Figure 8.** Sensitivity of fracture susceptibility to variations in  $\mu$  and  $C_0$ . Note the changes in scale along the x-  
358 axis between the plots.

359 The relative asymmetries of the skewed normal distributions for  $\mu$  and  $C_0$  have already been noted. Given  
360 their significant effect on  $S_f$  (high ranking in the tornado plot, Figure 7c), it is useful to explore how the  
361 skewness of these distributions might influence  $S_f$ . Figure 8 shows the results of repeated Monte Carlo  
362 sensitivity tests for  $\mu$  (Figure 8a, b) and  $C_0$  (Figure 8c, d). For friction, a positive skewness to higher values ( $\alpha$   
363  $> 0$ ) would tend to reduce  $S_f$  – i.e., faults would be less stable. For cohesion, the opposite is true – a negative  
364 skewness ( $\alpha < 0$ ) would make faults less stable to changes in  $P_f$ . These asymmetries are opposite to the ones  
365 used in the main Worked Example 2 and used by other workers (see Discussion). Widening the distributions  
366 for  $\mu$  or  $C_0$  by increasing their standard deviations (and retaining the original  $\alpha$  values) tends to broaden the  
367 distribution of predicted  $S_f$  with asymmetry to higher (i.e., more stable) values.

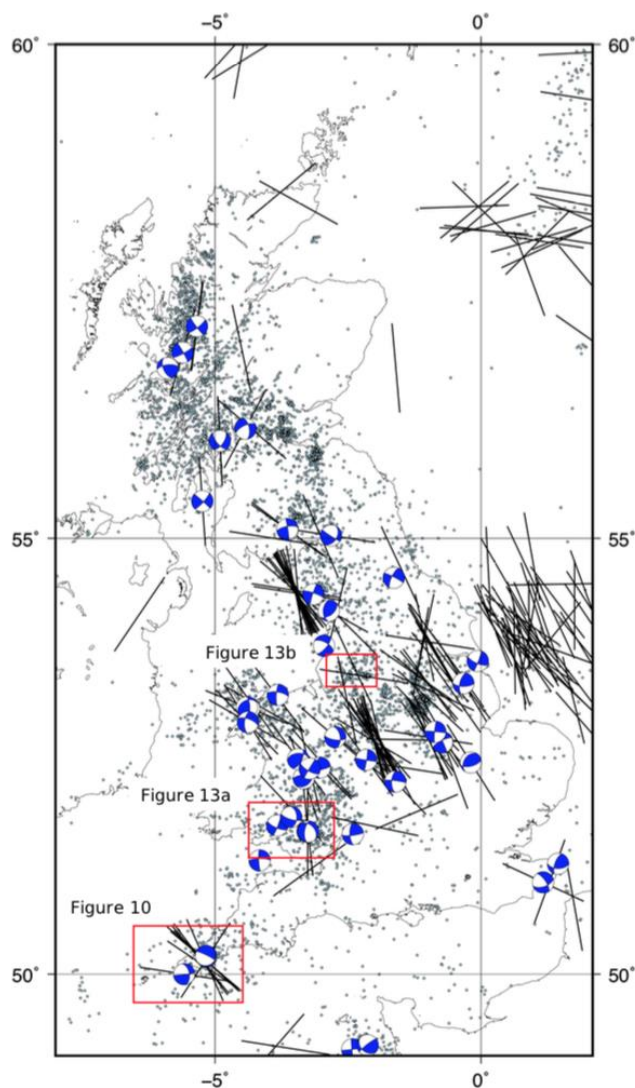
368

### 369 Case Studies

370 The case studies have been chosen to illustrate how a combined RSM/MC approach can be used to estimate  
371 the probability of slip on one or more faults, and to show that even with relatively good – i.e., complete –  
372 input data, these predictions highlight that industrial operations remain significantly hazardous, with a  
373 greater than 1 in 3 chance of slip on many faults across different settings. Selected specific aspects of the  
374 modelling and the visualisation of results are emphasised in each case study. Figure 9 shows a map of the UK  
375 with the case study areas marked, together with the locations of instrumentally-recorded earthquakes and  
376 their focal mechanisms (Baptie, 2010). Also shown are data from the World Stress Map database of 2016  
377 (Heidbach et al., 2018) indicating the orientation of the maximum horizontal stress. A basic observation from  
378 this map is the level of complexity and heterogeneity in the present day seismotectonics of the UK, reflecting



379 the variation in the subsurface geology. However, there is a broad prevalence of NW-SE trending  $\sigma_{Hmax}$   
380 directions and strike-slip earthquake mechanisms.



381

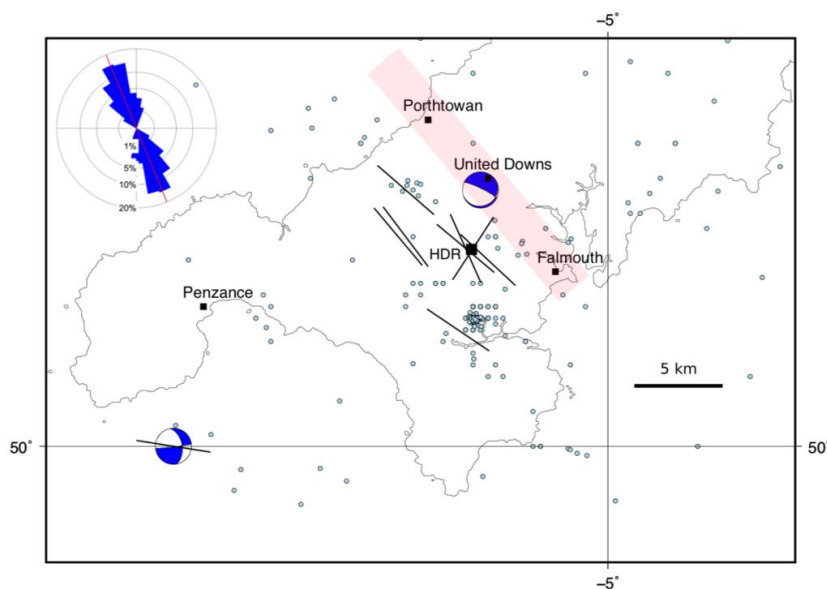
382 **Figure 9.** Map of most of the UK showing the locations of the selected case studies. Also shown: epicentres  
383 of seismicity (light blue dots; BGS catalogue – Musson, 1996), focal mechanisms (blue and white; Baptie,  
384 2010), and orientations of the maximum horizontal stress (black lines; World Stress Map data – Heidbach et  
385 al., 2018).

#### 386 1. Porthtowan Fault Zone in Cornwall, UK

387 The Porthtowan Fault Zone (PFZ) cuts the Carnmenellis granite in Cornwall in southwest England (Figure 10).  
388 This granite is a target for deep high-enthalpy geothermal energy due to its high radiogenic heat production  
389 (Beamish & Busby, 2016). Following the Hot Dry Rock (HDR) project in the 1980s (Pine & Batchelor, 1984;  
390 Batchelor & Pine, 1986), the United Downs pilot project has drilled two boreholes (UD-1, UD-2) to intersect  
391 the fault zone at depths of about 5,275 m and 2,393 metres, respectively, making UD-1 the deepest onshore  
392 borehole in the UK. The pilot project relies on shear-enhanced stimulation of pre-existing fractures (joints,



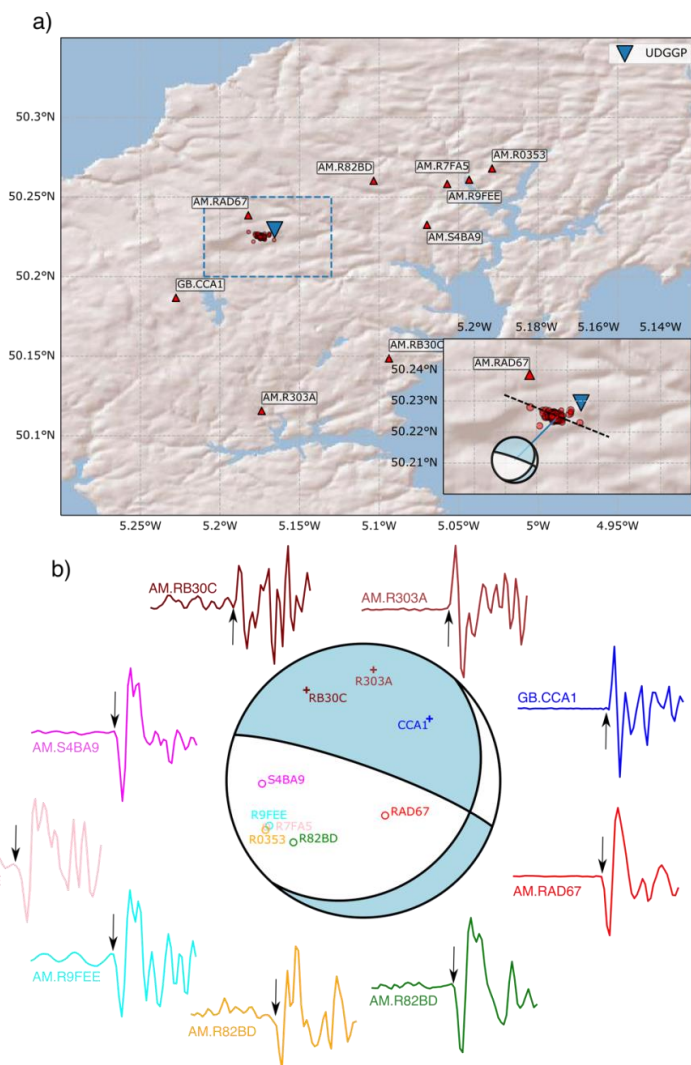
393 partially filled veins and faults) to drive fluid flow from the shallow injector (UD-2) to the deeper producer  
394 (UD-1). Temperatures at the base of UD-1 have been predicted at about 200°C (Ledingham et al., 2019).  
395 Shearing and downward flow of injected fluid was observed in boreholes as part of the earlier HDR project  
396 and tracked with measured microseismicity (Pine & Batchelor, 1984; Green et al., 1988; Li et al., 2018).



397  
398 **Figure 10.** Map of South West England showing: selected population centres, the United Downs deep  
399 geothermal pilot project and the former Hot Dry Rock project (black squares); epicentres of seismicity (light  
400 blue dots; BGS catalogue – Musson, 1996); focal mechanisms (blue and white; Baptie, 2010); and orientations  
401 of the maximum horizontal stress (black lines; World Stress Map data – Heidbach et al., 2018). Approximate  
402 trend and extent of the Porthtowan Fault Zone shown in pale red. Inset shows an equal area rose diagram  
403 with strikes of fault segments in the Porthtowan Fault Zone measured on BGS Falmouth sheet 352 ( $N=140$ ;  
404 circular mean strike= $158^\circ$ , circular standard deviation= $27^\circ$ ).

405 Figure 10 shows a map of SW England overlain with seismicity data from the BGS (Musson, 1996). The PFZ is  
406 poorly exposed inland, and runs NNW-SSE from Porthtowan on the north Cornish coast to Falmouth on the  
407 south coast (see inset rose diagram for strikes of constituent faults taken from the BGS Falmouth sheet 352).  
408 Overall, the fault zone is believed to dip steeply to the east at around  $80^\circ$ , but note that there is considerable  
409 variation in strike and dip of individual fault and fracture planes within the fault zone (Fellgett & Haslam,  
410 2021). The azimuth of the maximum horizontal stress is broadly NW-SE, with one exception trending NE-SW.



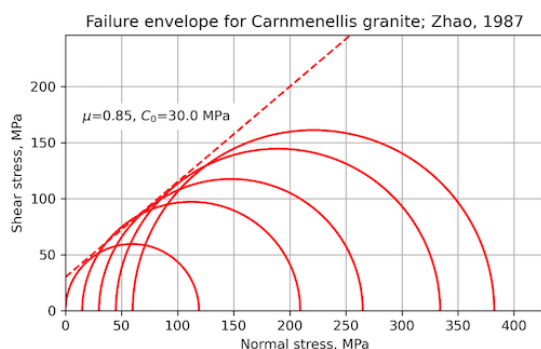
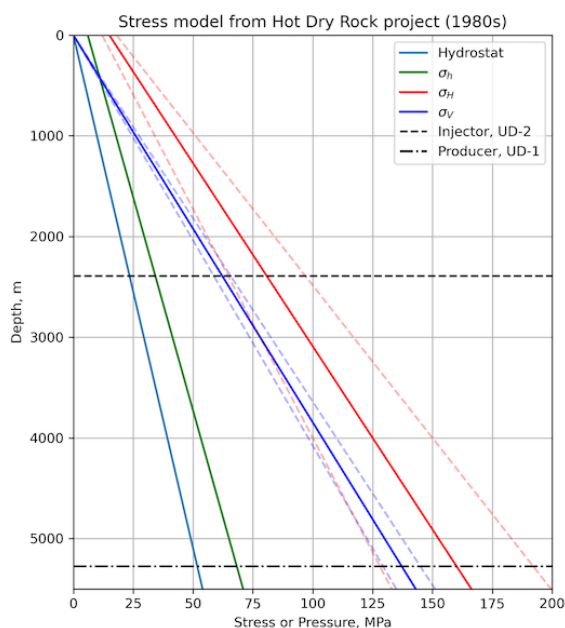


411

412 **Figure 11. a.** Red triangles show Raspberry Shake (network code: AM) and BGS (network code: GB) seismic  
 413 stations in Cornwall, with station names labelled. Seismicity during geothermal operations is indicated by red  
 414 circles. The inset shows a close-up of the area demarcated by the blue dashed line in the main map. The black  
 415 dashed line in the inset shows the broad WNW-ESE alignment in seismicity. **b.** Computed focal mechanism  
 416 for the 2020-09-30 11:44:01  $M_L$  1.6 induced earthquake. First-motions are plotted on the focal sphere with  
 417 “+” indicating positive polarity, and “o” for negative polarities. P-wave first-motions are plotted starting and  
 418 ending 0.3 seconds before and after the picked arrival, respectively, and are coloured in the same way as the  
 419 points on the focal sphere.

420





421

422 **Figure 12.** Constraints on input variables for the Porthtowan Fault Zone modelling. **a.** Stress-depth plot based  
 423 on data and equations from the Hot Dry Rock project in the Carnmenellis granite (Batchelor & Pine, 1986).  
 424 Also shown are the depths of the two wells in the pilot project at United Downs. **b.** Mohr diagram showing  
 425 data from laboratory mechanical tests of Zhao (1987) for brittle failure of Carnmenellis granite at 200°C.  
 426 Estimated Mohr-Coulomb failure envelope (dashed red line) is defined by  $\mu=0.85$ ,  $C_0=30$  MPa.

427 Detailed geomechanical analyses were performed in the Carnmenellis granite in the 1980s as part of the HDR  
 428 project, and these provide useful constraints on the variation of stress and fluid pressure with depth (Figure  
 429 12a; Batchelor & Pine, 1986). From these data, a strike-slip regime is most likely with  $\sigma_1 = \sigma_{Hmax}$  and  $\sigma_2 = \sigma_V$ ,  
 430 but note the uncertainties (based on quoted values in Batchelor & Pine, 1986): from around the depth of the  
 431 injector well at United Downs and deeper, a normal fault regime is also consistent with the data, i.e.,  $\sigma_1 = \sigma_V$   
 432 and  $\sigma_2 = \sigma_{Hmax}$ . Note that the earlier HDR project did not target a specific fault zone in the granite.

433 The thermo-mechanical properties of the Carnmenellis granite have been studied by Zhao (1987). Figure 12b  
 434 shows a Mohr diagram of data taken from Table 2.3 of Zhao (1987) for laboratory brittle failure tests  
 435 conducted at 200°C (the approximate temperature of the injector well at United Downs). From these data,  
 436 we have estimated a linear Mohr-Coulomb failure envelope defined by a friction coefficient of 0.85 and a



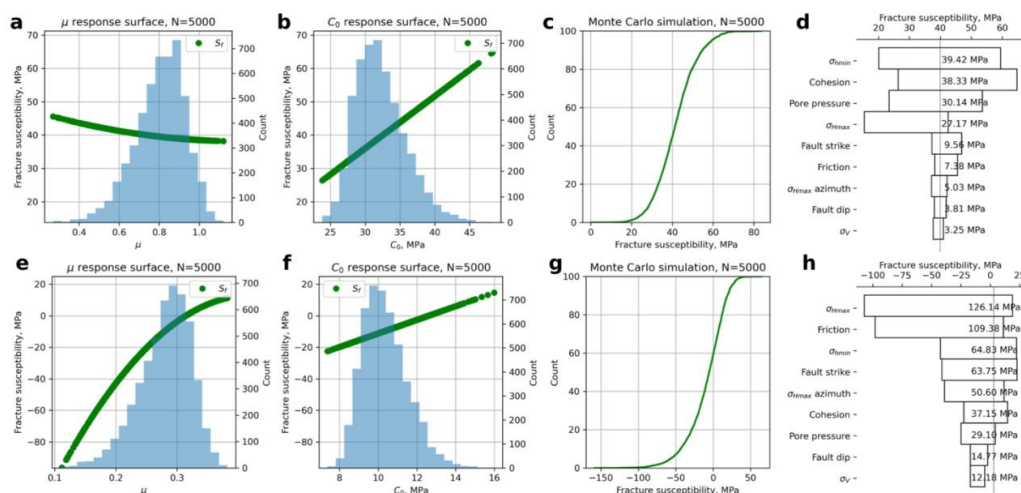
437 cohesive strength of 30 MPa. Cuttings from the boreholes at United Downs have been used to measure  
 438 friction coefficients of rocks within the PFZ, and values ranging between  $\mu=0.28-0.6$  were recorded (Sanchez  
 439 et al., 2020).

440 We present model results for fracture susceptibility in the PFZ as the plan at United Downs (and elsewhere  
 441 in the future) is to inject fluid into the fault zone in order to generate shear-enhanced permeability on pre-  
 442 existing fractures. Table 3 lists the input variable distributions used in the “base case” model for hydrostatic  
 443 pore fluid pressure in the fault zone and mechanical properties taken from laboratory tests of intact  
 444 Carnmenellis granite (Figure 12b). The modelled depth is chosen as 4 km, in between the depths of the UD-  
 445 1 and UD-2 wells.

Variable	Mean	Standard deviation ( $\kappa$ for Von Mises)	Units	Distribution	Comments
$\sigma_v$ , vertical stress	105.0	5.25 (5% of mean)	MPa	Normal	Lithostatic for depth of 4 km, assuming average rock density of $2650 \text{ kg m}^{-3}$ Batchelor & Pine, 1986
$\sigma_H$ , max. horizontal stress	125.0	25.0 (20% of mean)	MPa	Normal	Batchelor & Pine, 1986
$\sigma_h$ , min. horizontal stress	53.0	5.3 (10% of mean)	MPa	Normal	Batchelor & Pine, 1986
$P_f$ , pore fluid pressure	40.0	4.0 (10% of mean)	MPa	Normal	Hydrostatic for depth of 4 km, assuming average fluid density of $1000 \text{ kg m}^{-3}$
Azimuth of $\sigma_{Hmax}$	140	$\kappa=200$	°	Von Mises (circular Normal)	Batchelor & Pine, 1986
Fault strike	340	$\kappa=150$	°	As mapped	Digitised from BGS map
Fault dip	80.0	$\kappa=1000$	°	Von Mises (circular Normal), truncated at 0 and 90	
Friction, $\mu$	0.85	0.17 (20% of mean)	n/a	Skewed normal	$\alpha = -3$ i.e., skewed low
Cohesion, $C_0$	30.0	6.0 (20% of mean)	MPa	Skewed normal	$\alpha = +3$ i.e., skewed high

446

447 **Table 3.** Distributions of input variables used in the base case model of fracture susceptibility in the  
 448 Porthtowan Fault Zone.



449

450 **Figure 13.** Outputs from the Monte Carlo simulation of fracture susceptibility in the Porthtowan Fault Zone.  
 451 **a-d.** The response surface for the base case, with friction and cohesion estimated from the laboratory failure  
 452 tests of Zhao (1987), predicts positive fracture susceptibility i.e., a stable fault zone. The tornado plot (**d**)  
 453 shows that for relatively high values of cohesion (mode of  $C_0=30$  MPa in this case), the sensitivity to variations  
 454 in friction is slight. **e-h.** In contrast, the response surface for the ‘weak fault’ case, with reduced values of  
 455 friction and cohesion (mode of  $\mu=0.3$ , mode of  $C_0=10$  MPa), predicts fault zone instability i.e., overwhelmingly  
 456 negative values of  $S_f$ . The effect of friction on these predictions is now very strong, as shown in the shape of  
 457 the response surface for  $\mu$  (**e**) and in the ranking within the tornado plot (**h**).

458 The results from the Monte Carlo simulation of  $S_f$  for the PFZ are shown in Figure 13. For the base case, with  
 459 hydrostatic pore fluid pressure and a ‘strong fault’ (mode of  $\mu=0.85$ , mode of  $C_0=30$  MPa), the fault appears  
 460 unconditionally stable for the modelled *in situ* stress variations. The CDF shows almost exclusively positive  
 461 values of  $S_f$  up to about 60 MPa. Note that, for the input stress variations listed in Table 3, 22% of the MC  
 462 simulations produced an Andersonian normal fault regime ( $\sigma_1 = \sigma_v$ ), rather than a strike-slip ( $\sigma_2 = \sigma_v$ ) regime.

463 232 microseismic events with hypocentre depths of 4-5 km were detected by the BGS during geothermal  
 464 testing operations in 2021-2022 ([http://www.earthquakes.bgs.ac.uk/data/data\\_archive.html](http://www.earthquakes.bgs.ac.uk/data/data_archive.html); last accessed  
 465 23 July 2021). The largest earthquake induced by geothermal operations during this period occurred on 2020-  
 466 09-30 11:44:01, and had a local magnitude of  $M_l$  1.6, and was felt by residents in the area. This event was  
 467 well-recorded on a network of single-component Raspberry Shake stations (e.g. Holmgren & Werner, 2021)  
 468 and a single station of the BGS permanent monitoring network (Figure 11a). These stations offer excellent  
 469 azimuthal coverage of the geothermal seismicity, with the closest station lying only 2 km away (AM.RAD67).  
 470 Since no focal mechanisms have yet been documented for these induced earthquakes, we used recorded P-  
 471 wave first motions to compute a focal mechanism of the  $M_l$  1.6 event using the method of Hardebeck &  
 472 Shearer (2002). Take-off angles were computed using a 1D seismic velocity model for the Cornwall area  
 473 (<http://earthwise.bgs.ac.uk/index.php/OR/18/015> Table 4: Depth/crustal velocity models used in earth  
 474 quake locations; last accessed 23 July 2021). The best-fitting focal mechanism (Figure 11b) indicates either  
 475 normal faulting on a WNW-ESE steeply-dipping plane or strike-slip faulting on a shallow-dipping plane NE-  
 476 SW striking plane. Single event relocated epicentres reported by the BGS, which use arrivals from a local  
 477 dedicated microseismic monitoring array, show a NW-SE trend (Figure 11a), consistent with normal faulting  
 478 on a steeply east-dipping, WNW-ESE striking plane during this earthquake. Negative P-wave polarities were  
 479 recorded at AM.RAD67 for all  $M > 0$  events, indicating that the same fault plane was reactivated during many  
 480 of the induced events. The inferred fault plane is sub-parallel to the interpreted strike of the Porthtowan  
 481 Fault Zone that is targeted by the geothermal testing. This observed normal faulting mechanism is consistent  
 482 with our MC simulations (more than 1 in 5 of the predicted stress states were for normal faulting).

483



484 The response surface (green lines on Figure 13a-b) and the tornado plot of relative sensitivities of the input  
485 variables (Figure 13d) shows a positive dependence of  $S_f$  on the cohesion, and that variations in friction are  
486 relatively unimportant. If we reduce the strength of the modelled fault zone, by changing the input  
487 distributions of  $\mu$  and  $C_0$  to lower values – but with the same shape and skewness – the situation changes.  
488 The predicted fracture susceptibility is now much more strongly correlated with variations in friction, and  
489 less so with variations in cohesion. This can be explained by looking at the underlying formula for  $S_f$  (equation  
490 3), in particular the 2<sup>nd</sup> term on the RHS. If  $C_0 > \tau$  then the numerator of this term can be negative, producing  
491 a net positive term. However, if  $C_0 < \tau$  and  $\mu$  is small then this term is larger and negative. The important  
492 point is that the probability distribution of  $S_f$  (compare Figure 13c and 13g) is controlled by the *relative*  
493 magnitudes of  $\mu$  and  $C_0$ . In a weak fault zone, with low  $\mu$  and low  $C_0$ , the predictions are very sensitive to the  
494 value of friction. In a strong fault, the effect of  $\mu$  is less important. Thus, we need to know more about the  
495 relationship between  $\mu$  and  $C_0$  in fault rocks (see Discussion).

## 496 2. Coalfields in South Wales and Greater Manchester, UK

497 Scope exists to extract low enthalpy geothermal heat from disused coalmines in the UK (Farr et al., 2016),  
498 using either open- or closed-loop technology. Possible sites include the South Wales and Greater Manchester  
499 coalfields, where folded and faulted Coal Measures of Westphalian (upper Carboniferous) age have been  
500 mined for centuries, up until the 1980s. Initial plans for shallow mine geothermal schemes include *passive*  
501 dewatering which may not change the loading on faults by much. However, *active* dewatering schemes can  
502 promote ingress of deeper ground water (Farr et al., 2021), and as this fluid flow must be driven by gradients  
503 in fluid pressure, this could in turn lead to the instability of faults at greater depth. The models below are for  
504 a depth of 2 km.

505 The locations and orientations of faults have been taken from published BGS maps. For the South Wales  
506 coalfield (Figure 14a), we used the BGS Hydrogeology map of S Wales to map the traces of faults in the Coal  
507 Measures (Westphalian), and BGS 1:50k solid geology sheets over the same area to collect data on fault dips.  
508 For the Greater Manchester coalfield (Figure 14b), we used the BGS 1:50k solid geology sheets for Wigan,  
509 Manchester and Glossop. Faults were traced onto scanned images of the maps in a graphics package (Affinity  
510 Designer on an Apple iPad using an Apple Pencil). These fault trace maps were saved in Scalable Vector  
511 Graphics (.SVG) format, after deleting the original scanned image layer of the geological map. The saved .SVG  
512 files were read into FracPaQ (Healy et al., 2017) to quantify their orientation distributions (inset rose plots in  
513 Figure 14a and b). The fault trace maps were then overlain on maps containing historical seismicity and  
514 available focal mechanisms (from the public BGS catalogue; Musson, 1996) and the orientations of  $\sigma_{Hmax}$   
515 taken from the World Stress Map project (Heidbach et al., 2018).

516 In the South Wales coalfield 3,408 fault segments were traced, and the dominant trend is clearly NNW/SSE,  
517 but with important (and long) fault zones running ENE-WSW, such as the Neath and Swansea Valley  
518 Disturbances (Figure 14a). From cross sections, we measured 142 fault dips to help constrain the distribution  
519 of friction coefficients in these rocks (Figure 15b-c; see below), corrected for vertical exaggeration on the  
520 section line where necessary. Focal mechanisms in this area ( $n=4$ ) suggest that NNW/SSE and N/S faults are  
521 active in the current stress regime. Historical seismicity is widely, if unevenly, distributed with no obvious  
522 direct correlation to the surface mapped fault traces. For example, there are areas of intense surface faulting  
523 but no recorded historical seismicity, and vice versa – areas with abundant historical events but few mapped  
524 faults.

525 Around Greater Manchester 3,453 faults were traced, and the dominant trend is NW/SE, but E/W faults are  
526 also present (Figure 14b). From cross sections, we measured 89 faults to help constrain the distribution of  
527 friction coefficients in these rocks (Figure 15d-e; see below). Historical seismicity is again widely, if unevenly,  
528 distributed with few obvious direct correlations to the surface mapped fault traces. However, there was an  
529 earthquake swarm in 2002-2003 which comprised more than 100 events, with a maximum local magnitude  
530 of 3.9. Calculated focal depths were 1 – 3 km, although these have large uncertainties (Walker et al., 2003).  
531 The World Stress Map database has the orientation of  $\sigma_{Hmax}$  trending WNW/ESE in this area (Figure 12b),  
532 based on the focal mechanisms for local events in the 2002-2003 swarm (this is distinct from the regional



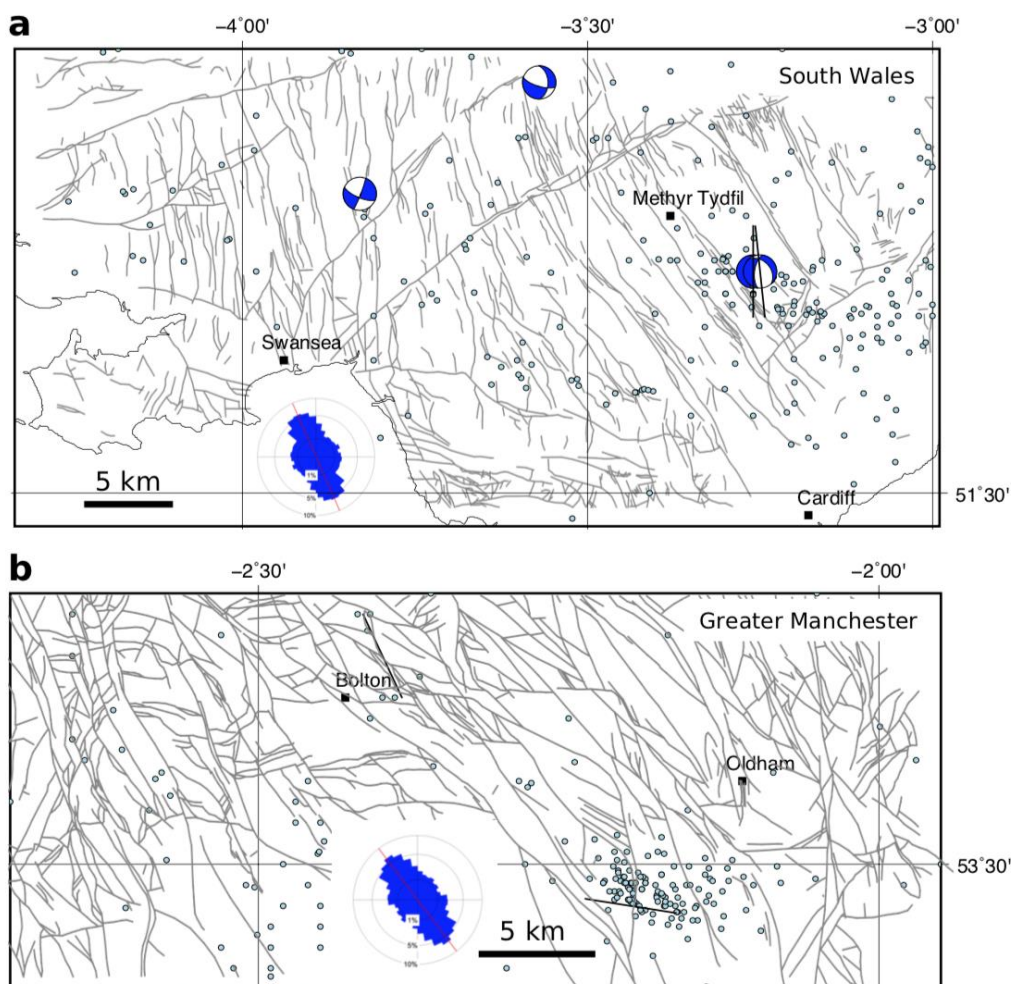
533 trend of  $\sigma_{Hmax}$  which is more NW/SW e.g., Williams et al., 2016). These observations suggest that faults  
534 oriented more nearly E/W are more likely to slip in the current stress regime.

535 There are no published geomechanical analyses for the variation of stress with depth for either of these two  
536 areas. To constrain the depth dependence of stress, we have used larger scale syntheses of stress for onshore  
537 UK produced by the BGS (e.g., Kingdon et al., 2016; Fellgett et al., 2018). The stress-depth plot in Figure 15a  
538 has been constructed using the data shown in Fellgett et al. (2018), and shows that, in general, a strike-slip  
539 fault regime with  $\sigma_1 = \sigma_{Hmax}$  is most likely. However, given the known uncertainties in these data, a normal  
540 fault regime ( $\sigma_1 = \sigma_v$ ) cannot be ruled out, especially at depth. Note that the stress-depth data shown in  
541 Fellgett et al. (2018) and used in Figure 15a are compiled from different areas, and remain untested for the  
542 specific areas shown in this paper. The azimuth of  $\sigma_{Hmax}$  is known to vary across the UK ranging from ~130 to  
543 ~170 (Baptie et al., 2010; Becker & Davenport, 2001).

544 Despite the economic and historical significance of the Coal Measures, there are no published datasets of  
545 laboratory measured friction or cohesion for either intact rocks or their faulted equivalents (although data  
546 may exist in proprietary company records). Data for specific units of interest does exist, e.g., for the  
547 Oughtibridge Ganister, a seat earth in the Coal Measures (Rutter & Hadizadeh, 1991); and the Pennant  
548 Sandstone, a rare marine sandstone unit (Cuss et al., 2003; Hackston & Rutter, 2016), but a systematic  
549 analysis of the volumetrically dominant sandstone, siltstone and mudstone formations is notably absent.  
550 Instead, we use the measured dips of faults in the Coal Measures as a proxy for the coefficient of sliding  
551 friction, using the relationship

$$552 \quad \mu = 1/\tan(\pi - 2\beta) \quad \text{equation 14}$$

553 where  $\beta$  is the angle between the fault plane and  $\sigma_1$  at failure (Jaeger et al., 2009; Carvell et al., 2014). Such  
554 a calculation assumes Mohr-Coulomb failure and that the current dip of the fault is reasonably close to the  
555 dip at failure in the post-Westphalian deformation of the coalfields. For measured fault dips  $< 45^\circ$ , we assume  
556 that  $\sigma_1$  was horizontal (Andersonian thrust/reverse fault regime) and for fault dips  $\geq 45^\circ$  we assume  $\sigma_1$  was  
557 vertical (Andersonian normal fault regime). In practice, some of these faults probably originated as strike-slip  
558 faults (i.e., with a sub-vertical dip and  $\sigma_2$  vertical), and some of their dips have almost certainly been modified  
559 by compaction since their formation. However, this method of estimating the likely range of friction  
560 coefficients from measured dips remains simple to apply and useful to first order, in the absence of better  
561 data. From the dip data, the calculated friction coefficients vary between 0.0 and 6.0 for South Wales, and  
562 between 0.35 and 2.0 for Greater Manchester (Figures 15c and e, respectively).

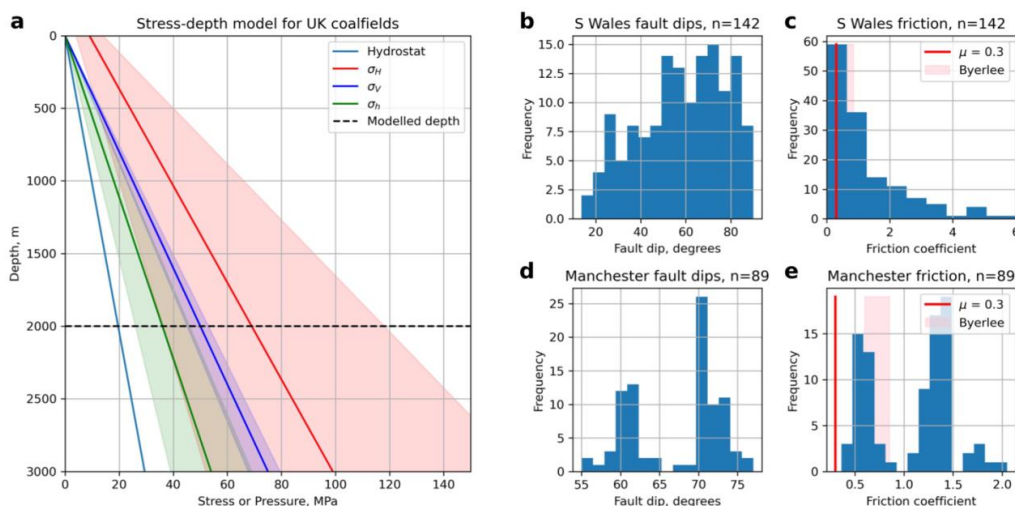


563

564 **Figure 14.** Maps of selected UK coalfields (suggested sites of shallow mine geothermal energy) showing:  
565 selected population centres (black squares); epicentres of seismicity (light blue dots; BGS catalogue –  
566 Musson, 1996); focal mechanisms (blue and white; Bapchie, 2010); and orientations of the maximum  
567 horizontal stress (black lines; World Stress Map data – Heidbach et al., 2018). Inset equal area rose diagrams  
568 show orientations of mapped faults. **a.** South Wales area. Faults in the Coal Measures taken from the BGS  
569 Hydrogeological Map of South Wales (1:125k) ( $n=3,408$ ), with a circular mean strike= $156^\circ$  and a circular  
570 standard deviation= $65^\circ$ . **b.** Greater Manchester area. Faults in the Coal Measures taken from the BGS 1:50k  
571 sheets Wigan, Manchester and Glossop ( $n=3,453$ ), with a circular mean strike= $143^\circ$  and a circular  
572 standard deviation= $64^\circ$ .

573 Based on the values of sliding friction calculated from measured fault dips across both coalfields a threshold  
574 stability value of  $\mu=0.3$  is taken as a reasonable lower bound for faulted rock. This is the value used to  
575 compare with predicted slip tendencies calculated for each fault. For  $T_s > 0.3$ , the fault is deemed unstable,  
576 for  $T_s \leq 0.3$  it is stable.





577

578 **Figure 15.** Constraints on input variables for the coalfield modelling of slip tendency. **a.** Stress-depth plot  
 579 based on data from onshore UK (after Fellgett et al., 2018). Also shown is the modelled depth of 2 km. **b-e.**  
 580 Histograms of fault dips measured cross-sections on published BGS 1:50k maps of South Wales and Greater  
 581 Manchester, and calculated values of friction coefficients derived from these dips assuming Mohr-Coulomb  
 582 failure. Byerlee friction ( $\mu=0.6-0.85$ ) shown as shaded pink box. Modelled critical values of friction ( $\mu=0.3$ )  
 583 shown by red lines.

584

Variable	Mean	Standard deviation ( $\kappa$ for Von Mises)	Units	Distribution	Comments
<b>South Wales coalfield <math>T_s</math> model, depth=2 km</b>					
$\sigma_v$ , vertical stress	50.0	3.75 (5% of mean)	MPa	Normal	Lithostatic for depth of 2 km, assuming average rock density of $2500 \text{ kg m}^{-3}$
$\sigma_h$ , max. horizontal stress	70.0	14.0 (20% of mean)	MPa	Normal	After Fellgett et al., 2018
$\sigma_h$ , min. horizontal stress	35.0	3.5 (10% of mean)	MPa	Normal	After Fellgett et al., 2018
Azimuth of $\sigma_{Hmax}$	160	$\kappa=200$	°	Von Mises (circular Normal)	After Fellgett et al., 2018; Baptie, 2010; WSM, 2016
Fault strike	-	-	°	As mapped	Digitised from BGS Hydrogeology sheet
Fault dip	n/a	$\kappa=25$	°	Von Mises (circular Normal), truncated at 0 and 90	Fitted to data taken from cross-sections on BGS 1:50k sheets 229-231, 247-249, 263, 263
<b>Greater Manchester coalfield <math>T_s</math> model, depth=2 km</b>					
$\sigma_v$ , vertical stress	50.0	7.5 (5% of mean)	MPa	Normal	Lithostatic for depth of 2 km, assuming average rock density of $2500 \text{ kg m}^{-3}$





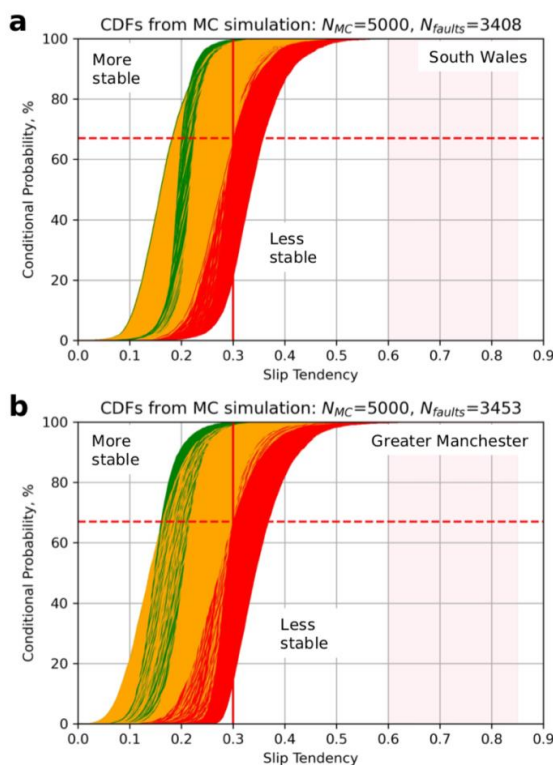
$\sigma_h$ , max. horizontal stress	70.0	14.0 (20% of mean)	MPa	Normal	After Fellgett et al., 2018
$\sigma_h$ , min. horizontal stress	35.0	3.5 (10% of mean)	MPa	Normal	After Fellgett et al., 2018
Azimuth of $\sigma_{Hmax}$	145	$\kappa=200$	°	Von Mises (circular Normal)	After Fellgett et al., 2018; Baptie, 2010; WSM, 2016
Fault strike	-	-	°	As mapped	Digitised from BGS 1:50k sheets 84-86
Fault dip	60.0	$\kappa=200$	°	Von Mises (circular Normal), truncated at 0 and 90	Fitted to data taken from cross sections on BGS 1:50k sheets 84-86

585

586 **Table 4.** Distributions of input variables used to model slip tendency in the coalfields of South Wales and  
 587 Greater Manchester.

588 Predictions of conditional probability for fault slip have been calculated for all faults in both coalfields using  
 589 slip tendency as the chosen measure: in the absence of detailed pore fluid pressure constraints or estimates  
 590 of cohesive strength, it is hard to justify modelling the fracture susceptibility. Slip tendency provides a first  
 591 order estimate of fault stability. A quadratic response surface was constructed for each coalfield using the  
 592 full range of measured fault strikes and dips, and the input variable distributions listed in Table 4 and  
 593 constrained by the data in Figure 15. Monte Carlo simulations ( $N_{MC}=5,000$ ) were run for each mapped fault  
 594 segment with the other input variables drawn from their respective distributions. Note that the principal  
 595 stresses used were the same for both coalfields, for a depth of 2 km (see Table 4), but the azimuth of  $\sigma_{Hmax}$   
 596 was varied to reflect the regional differences reported by other authors (Becker & Davenport, 2001; Baptie,  
 597 2010), and the recorded focal mechanisms.

598 Output CDFs for all faults in both coalfields are shown in Figure 16. For South Wales ( $N=3,408$  faults),  
 599 approximately 46% of faults are predicted to have a 1 in 3 chance of being unstable (i.e.,  $T_s > 0.3$ , shown in  
 600 red), and 42% of faults are predicted to have a 1 in 10 chance of being unstable (shown in amber). For Greater  
 601 Manchester ( $N=3,453$  faults), approximately 46% of faults are predicted to have a 1 in 3 chance of being  
 602 unstable (i.e.,  $T_s > 0.3$ , shown in red), and 54% of faults are predicted to have a 1 in 10 chance of being  
 603 unstable (shown in amber).

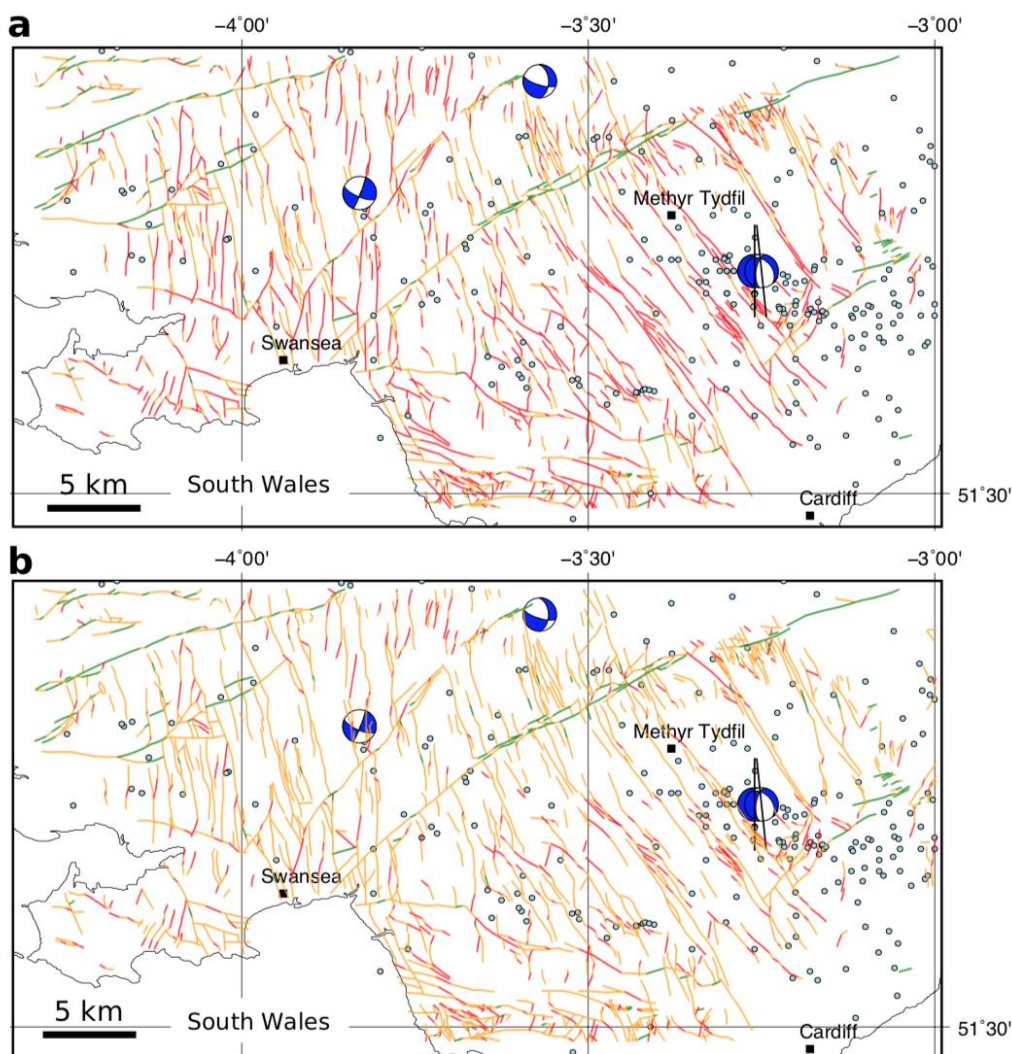


604

605 **Figure 16.** Output from the Monte Carlo modelling of slip tendency in UK coalfields. For slip tendency, more  
606 stable faults skew towards the left (low  $T_s$ ), less stable faults skew to the right (high  $T_s$ ). **a.** CDFs of predicted  
607 slip tendency for each mapped fault in South Wales. **b.** CDFs of predicted slip tendency for each mapped fault  
608 in Greater Manchester. Colour coding of CDFs – red: >33% chance of exceeding threshold friction ( $\mu=0.3$ ,  
609 vertical red line), amber: >1% and <33% chance, green: < 1% chance. Range of Byerlee friction shown by pink  
610 shading.

611 The results from the RSM/MC modelling shown in the CDFs are replicated in map view in Figures 17 and 18.  
612 Each fault segment is colour coded using the same heuristic applied in the CDF: red faults have a conditional  
613 probability of at least 33% of their slip tendency exceeding the chosen threshold value of fault rock friction  
614 ( $\mu=0.3$ ), amber (orange) faults have a 1-33% chance, and green faults have a less than 1% chance of being  
615 unstable.

616 For South Wales, the general pattern of the predictions is consistent with the recorded focal mechanisms  
617 (Figure 17a). The most likely fault segments to slip (coloured red) are those oriented either NNW/SSE or N/S,  
618 corresponding with one of the nodal planes in each of the focal mechanisms. Faults trending ENE/WSW, such  
619 as the Neath Disturbance, are predicted to have low probability of slip in the modelled stress regime (green).  
620 Note that the Swansea Valley Disturbance trends ENE/WSW as a fault zone, but the constituent fault  
621 segments are variously oriented including elements that trend NE/SW, and these are marked in red (high  
622 probability of slip). Blenkinsop et al. (1986) noted that this fault zone may in fact have a shallow dip at depth,  
623 which is not covered by the dip distribution used in our modelling, so further work is required here. The  
624 location with the most recorded events lies to the SE of Merthyr Tydfil, and this corresponds to an area with  
625 many mapped faults trending NW/SE marked with a high probability of slip, and consistent with two of the  
626 focal mechanisms.



627

628 **Figure 17.** Output from the Monte Carlo modelling of slip tendency in South Wales coalfield. **a.** Colour-coded  
629 fault map showing conditional probability of slip for each mapped fault. This map shows the unweighted  
630 values, as shown on the CDFs in Figure 14a. **b.** Colour-coded fault map showing conditional *weighted*  
631 probability of slip for each mapped fault. The weighted probability is calculated by multiplying the probability  
632 from the CDF in Figure 14a by the normalised fault smoothness, ranging from 1.0 for a perfectly straight (i.e.,  
633 smooth) fault, and tending to 0.0 for a rough fault. Colour coding of CDFs – red: >33% chance of exceeding  
634 threshold friction ( $\mu=0.3$ ), amber: >1% and <33% chance, green: < 1% chance.

635

636

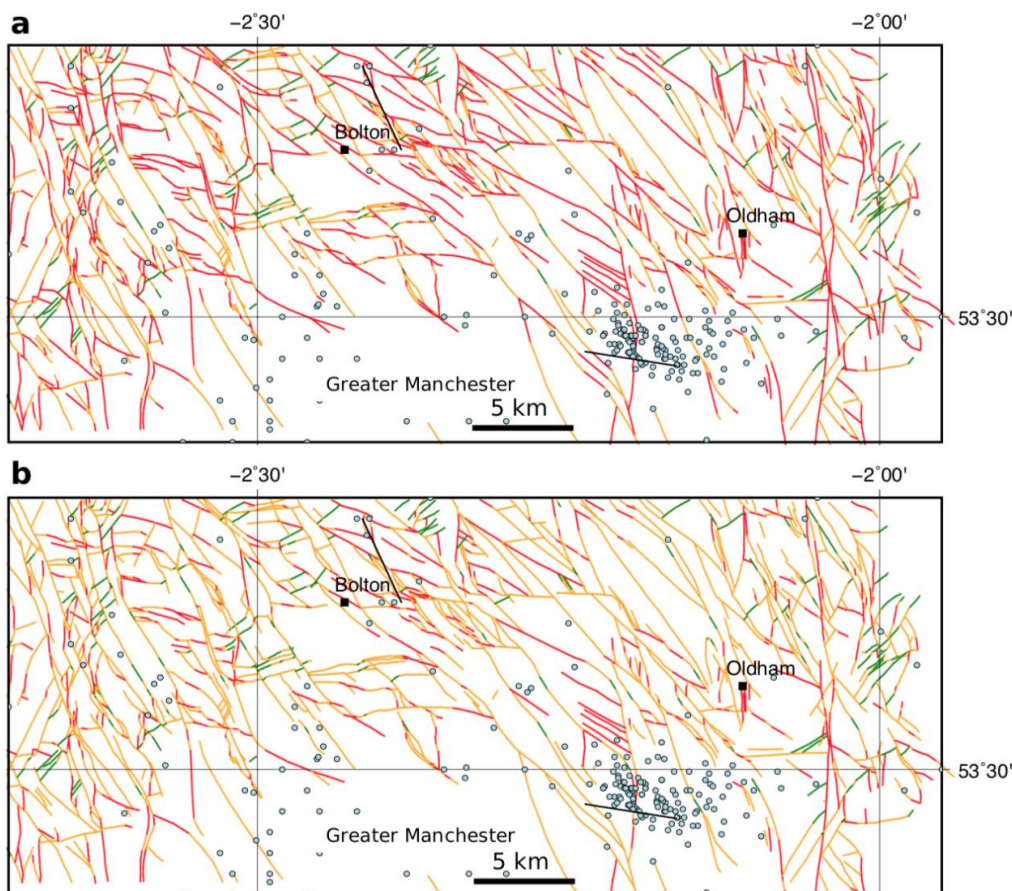
637

638

639



640 For Greater Manchester (Figure 18a), the simulation suggests that many faults are likely to slip in the  
641 modelled stress regime, even though the recorded seismicity is generally sparse. The exception is the area  
642 of the 2002-2003 swarm near Manchester city centre. Here the recorded events coincide with mapped  
643 surface faults trending WNW/ESE and predicted as likely to slip (red).



644  
645 **Figure 18.** Output from the Monte Carlo modelling of slip tendency in Greater Manchester coalfield. **a.**  
646 Colour-coded fault map showing conditional probability of slip for each mapped fault. This map shows the  
647 unweighted values, as shown on the CDFs in Figure 14b. **b.** Colour-coded fault map showing conditional  
648 *weighted* probability of slip for each mapped fault. The weighted probability is calculated by multiplying the  
649 probability from the CDF in Figure 14b by the normalised fault smoothness, ranging from 1.0 for a perfectly  
650 straight (i.e., smooth) fault, and tending to 0.0 for a rough fault. Colour coding of CDFs – red: >33% chance  
651 of exceeding threshold friction ( $\mu=0.3$ ), amber: >1% and <33% chance, green: < 1% chance.

652

## 653 Discussion

### 654 *Stress, pressure, and temperature*

655 The simulations described in this paper all critically depend on our knowledge of the *in situ* stress tensor. We  
656 can constrain some of the components of this tensor better than others. The vertical stress ( $\sigma_v$ ) is usually the  
657 best constrained, a reflection of its derivation from the borehole density logs sampled at sub-metre  
658 resolution. Our estimates of the horizontal stresses,  $\sigma_{Hmax}$  and  $\sigma_{Hmin}$ , remain poorly constrained. Even in cases





659 with relatively good data, e.g., from borehole leak-off tests (LOTs) and formation integrity tests (FITs), the  
660 “data density” for these stress components is generally sparse (compared to  $\sigma_v$ ), and we are stuck with  
661 significant uncertainties. And these uncertainties matter, as shown by this study and previous work (e.g.,  
662 Chiaramonte et al., 2008; Walsh & Zoback, 2016). The fundamental dependence of shear failure on  
663 differential stress inherent in the Mohr-Coulomb failure criterion is reflected in the high ranking of stress  
664 tensor components in the tornado plots shown in this study. Also, larger uncertainties in stress components  
665 mean that the Andersonian regime may flip from the default “average” assumption to another orientation:  
666 e.g., an apparently strike-slip regime may in fact include a significant proportion of normal fault possibilities  
667 (>20% in the case of the Porthtowan Fault Zone shown here). One way to improve our knowledge of the  
668 stress tensor, and especially the azimuth of  $\sigma_{Hmax}$  would be to exploit richer catalogues of seismicity to  
669 produce more focal mechanisms for natural or induced events. Most countries would benefit from better –  
670 i.e., more widespread and higher resolution – continuous seismic monitoring. While this may be expensive  
671 with top of the range broadband equipment, citizen science devices, such as the Raspberry Shake, offer a  
672 low cost and viable alternative (Cochran, 2018; Anthony et al., 2019; Hicks et al., 2021; Holmgren & Werner,  
673 2021). Our study shows how Raspberry Shake data are effective for computing focal mechanisms. Analysis  
674 of more events would allow stress inversions to be performed on the data measured by these devices,  
675 especially when they are combined in *ad hoc* arrays to improve signal to noise ratios.

676 Pore fluid pressures at depth are also poorly known, even for a country like the UK with a long tradition of  
677 geological (and geophysical) science and rich history of mining and drilling into the crust. Most importantly,  
678 our knowledge of measured *in situ* pore fluid pressures in and around fault zones is generally poor.  
679 Theoretical predictions and model simulations abound, but direct measurements of this key parameter are  
680 almost non-existent. We need to know the actual limits of pore fluid pressures in fault zones, and their likely  
681 spatial and temporal variation over a fault plane throughout the seismic cycle. The situation is complicated  
682 by the finer scale structure of fault zones. Fault zones in low porosity and/or crystalline rocks (such as granite)  
683 can be divided into one or more narrow cores defined by fine grained fault rocks (gouges, cataclasites)  
684 surrounded by wider damage zones of more or less fractured rock. Permeability may be low in and across  
685 the core(s) and higher in the damage zones (Caine et al., 1996; Faulkner et al., 2010). In high porosity and/or  
686 granular rocks (such as sandstone), fault zones may be simpler, with a fine grained fault rocks along narrow  
687 fault planes forming an effective fluid seal (Wibberley et al., 2008) These differences in the physical  
688 characteristics of the fault zones have consequences for the distribution of dynamic pore fluid pressures,  
689 which remain poorly known in detail.

690 The work described in this paper has ignored the effects of temperature. However, thermoelastic stress may  
691 be more important than poroelastic stress by a factor of 10 (Jacquey et al., 2015). In short, colder injected  
692 water may increase the chance of slip on a given fault. In the UK, our knowledge of the subsurface  
693 temperature field is increasing (Beamish & Busby, 2016; Farr et al., 2021), but we need more data, and again,  
694 especially from faulted rocks.

#### 695 *Faults*

696 An implicit assumption in all of the modelling performed in this paper (and many others) is that we know  
697 something about the fault which may slip: i.e., we can only quantify risk on known faults. There will, in  
698 general, be many more unmapped faults in the subsurface, and these may be the ones most likely to slip due  
699 to a change in loading (of either *in situ* stress or fluid pressure). This is apparent in the maps for the coalfields  
700 shown in this paper in terms of the relative lack of correspondence between the surface mapped fault traces  
701 and the locations of recorded earthquakes. Some of this “mismatch” could be explained by the dip of the  
702 faults measured at the surface, but not all. Moreover, there are areas of apparently intense surface faulting  
703 and no recorded seismicity, and vice versa (recorded seismicity but no mapped surface faults). Some advance  
704 could be made to address this problem with the recognition that each recorded seismic event documents a  
705 fault plane, assuming that a double couple focal mechanism implies fault slip rather than dilation from dyke  
706 emplacement or other mechanisms. And therefore the 3D position of each focal mechanism points to at least  
707 part of a subsurface fault. The challenge then lies in mapping these seismic event fault planes into a viable  
708 fault network. Better data (i.e., higher spatial resolution and extending to smaller event magnitudes) from



709 more dense arrays of seismometers would help with this task, as for the refinement of stress estimates noted  
710 above.

#### 711 *Rock properties*

712 The importance of good data on rock properties has been emphasised above, in the Worked Example for  
713 fracture susceptibility and in the case study for the Porthtowan Fault Zone. In general, we need more and  
714 better data on coefficients of friction and cohesive strength, especially for the target formations of  
715 decarbonisation operations. Moreover, we need data for the intact *and* faulted rocks. We also need better  
716 constrained correlations among rock properties. A widely used method in oil and gas is to derive estimates  
717 of friction coefficient and UCS from wireline log datasets measuring porosity, slowness (velocity) or elasticity  
718 e.g., Chang et al., 2006. However, as noted by these authors, the correlations are strictly valid only for the  
719 specific formations tested in the laboratory, and even then, the uncertainties remain large. A further issue is  
720 the tendency to average wireline log derived estimates over a depth interval, when for most sections of crust  
721 this is the direction in which rock properties are expected to vary most rapidly. The Porthtowan Fault Zone  
722 example above highlighted another issue: the relative impact of cohesion and friction on the predicted  
723 stability depends on the magnitude of the cohesion in relation to the shear stress on the fault. For low  
724 cohesion values, the constraints on friction become much more important. We need systematic  
725 investigations of frictional behaviour at low cohesive strength. We need detailed systematic correlations  
726 among rock properties, especially for faulted crystalline basement rocks.

727 Collecting more laboratory data is no panacea, evidenced by the well-aided concerns over how we up-scale  
728 rock properties and behaviours from mm- and cm-sized samples to whole fault zones. But calibrations and  
729 correlations from careful, systematic laboratory data remain the cornerstone of estimating the key *in situ*  
730 values. An interesting new focus would be to explore the nature of the skewness in mechanical property  
731 datasets: why should friction coefficients skew low, and cohesive strength skew high?

732 The utility of the Mohr-Coulomb criterion used in this paper is largely down to its mathematical simplicity,  
733 i.e., linearity and only two parameters (friction and cohesion). Other criteria are perfectly viable and could  
734 easily be added to the pfs Python code, but some other failure criteria lack a clear mapping between their  
735 parameters and the mechanics of sliding on rock surfaces.

#### 736 *Applicability of $T_s$ , $T_d$ and $S_f$ for quantifying risk*

737 A valid question is to ask whether any of these widely used measures of fault stability are, in fact, useful in  
738 practical terms at the scale of faults on maps. All three measures focus on the simplified mechanics of slip on  
739 a specific fault plane, with a fixed orientation and with specific rock properties. But seismic hazard is not  
740 isolated at the level of single fault planes. Faults occur in patterns or networks, more or less linked together.  
741 Geometrical factors may be more important than the specifics of either the *in situ* stress or the rock  
742 properties, at the scale of observation. The observational record shows that bigger fault zones are the sites  
743 of bigger earthquakes, and they are also the locus of most displacement in a given network. Conversely,  
744 smaller faults host smaller seismic events, and accrue less overall displacement (Walsh et al., 2001). To begin  
745 to address this issue, we can weight the conditional probabilities of slip for a specific fault segment by a  
746 dimensionless normalised factor derived from the total length of the fault: e.g.,  $w_{size} = l_s / l_t$  where  $l_s$  is fault  
747 segment length and  $l_t$  is fault trace length. An alternative, but related idea, is that of the relationship between  
748 fault smoothness (or inversely, roughness) and fault maturity, and therefore seismic hazard (Wesnouslyk  
749 et al., 1988). The most seismically active faults are not only, or necessarily, the largest ones in their network,  
750 but tend to be the smoothest or most connected, reflecting the coalescence of fault segments through time  
751 and the removal of asperities through repeated slip events (Stirling et al., 1996). Therefore, we can weight  
752 the conditional probabilities of slip by a dimensionless factor of smoothness:  $w_{smooth} = l_{straight} / \sum(l_s)$ , where  
753  $l_{straight}$  is the straight line length between fault end points, which is 1.0 for a perfectly smooth fault with all  
754 segments parallel and connected, and tends to 0.0 for rough, complex fault traces. Examples of the effect of  
755 these smoothness weightings applied to the conditional probabilities are shown in Figures 17b and 18b for  
756 the UK coalfield faults. The net effect is to reduce the number of most risky faults (shown in red) by about  
757 half. These approaches are the subject of further work and testing.

758



## 759 Summary

760 In this paper, we have described and explained the Response Surface Methodology and shown how it can be  
761 combined with a Monte Carlo approach to generate probabilistic estimates of fault stability using published  
762 measures of slip tendency, dilation tendency and fracture susceptibility. Simulations show that a quadratic  
763 response surface always generates a better fit to the input variables in comparison to a linear surface, at the  
764 cost of larger matrices (more computer memory) and longer run times. Worked examples to calculate  $T_s$  and  
765  $S_f$  with synthetic input distributions show how the quadratic response surfaces vary for each input parameter.  
766 For slip and dilation tendency, the primary dependence is (as expected) on the maximum differential stress,  
767 and therefore the maximum and minimum principal stresses of the *in situ* stress tensor, with a lesser  
768 dependence on the fault orientation. For fracture susceptibility, the situation is more complex: if cohesion is  
769 relatively high,  $S_f$  is mainly dependent on the *in situ* stresses and cohesion. But if cohesion is low – quite likely  
770 in fault zones – then the dependence of  $S_f$  on friction is much more significant. This is a key finding: the  
771 relative sensitivity of the input variables on the response surface varies with the absolute value of the  
772 variables.

773 Sensitivity tests were used to assess how the shapes of different input distributions affect the predictions of  
774 fault stability. Varying the spread of symmetric (normal, Gaussian) distributions of input variables has a  
775 significant effect on the predictions, and this mirrors the reality of uncertainties in, for example, the principal  
776 stresses in a standard geomechanical analysis. As noted above, the vertical stress is often well constrained  
777 and has a lower relative standard deviation (say, 5% of the mean) than either the maximum or minimum  
778 horizontal stresses (typically 15-20% of their mean value). The shape and spread of skewed (asymmetric)  
779 distributions of rock properties (friction and cohesion) is also important. The direction of skewness is  
780 described by the sign of the parameter  $\alpha$  for the skewed normal distributions used in this paper to model  
781 variations in rock properties. Friction is modelled with a negative skewness towards lower values, whereas  
782 cohesion is modelled with positive skewness towards higher values, but systematic laboratory data are  
783 needed to verify these assumptions. This will require a statistically significant number of repeat tests for each  
784 property on quasi-identical samples of the same rock.

785 Case studies of three different locations demonstrated how a probabilistic approach can provide a useful  
786 assessment of fault stability, including which of the input variables are the most important for a given  
787 combination of *in situ* stress, fault plane orientation and rock properties. This then enables greater focus on  
788 improving the estimates of the key variables, and the relationships between them. For the Porthtowan Fault  
789 Zone in Cornwall, the modelling in this paper shows that we need more data for, and a better understanding  
790 of the relationship between, coefficients of friction and cohesive strength, especially at low values of friction  
791 (i.e., less than the Byerlee range of 0.6-0.85) to be expected in fault zones. For the coalfields in South Wales  
792 and Greater Manchester, model outputs show how predictions of fault stability can be weighted by a simple  
793 index of fault smoothness to begin to allow for the effects of geometrical weakening within the fault system  
794 as whole, rather than focusing on each individual fault plane taken in isolation.

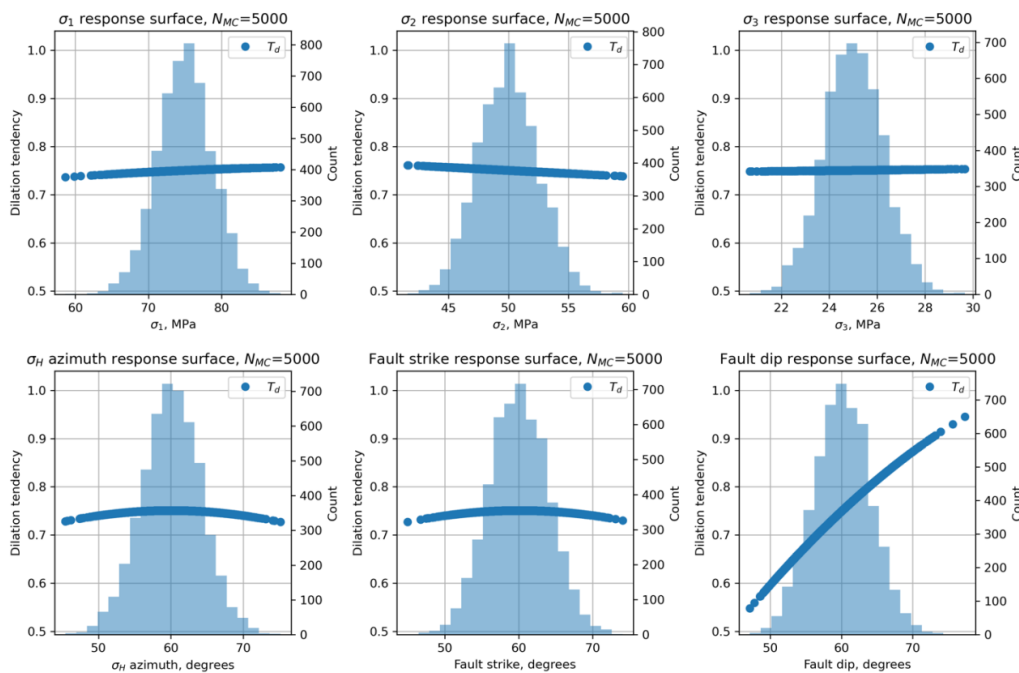
795 It's obvious that uncertainty in the input parameters must translate into uncertainty in the output  
796 predictions. By combining a Response Surface Methodology with a Monte Carlo approach to the  
797 quantification of fault stability, we can explore, understand, and quantify how differing degrees of  
798 uncertainty among the input parameters feed through to uncertainty in the predicted stability measure.  
799 Response surfaces and tornado plots can help to identify which parameters are the most important in a  
800 particular analysis. Given our current state of knowledge of stress, fault orientations and fault rock  
801 properties, probabilistic estimates and iterative modelling are useful approaches to begin to de-risk the  
802 energy transition. Free, open source software to perform these analyses, such as the Python package pfs,  
803 can help to encourage their wider adoption and further refinement ("given enough eyeballs, all bugs are  
804 shallow"; Raymond, 2001). The deployment of abundant and relatively low-cost citizen science seismometers  
805 (e.g., Raspberry Shakes) could synergise two critical issues: the wider involvement of the public into open  
806 science debates about risk and the simultaneous collection of better data to constrain the local stress field.  
807 The energy transition and decarbonisation are urgent and essential tasks: we will only be successful if we  
808 manage to balance public perceptions of risk with the technical challenges inherent to the exploitation of  
809 faulted rock.





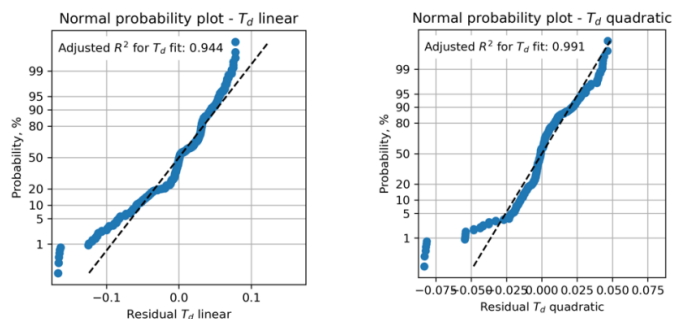
811 **Appendix A – Dilation tendency plots**

812 For completeness, we include the analysis of dilation tendency ( $T_d$ ) for the same synthetic input dataset used  
 813 to calculate slip tendency ( $T_s$ ) – i.e., input variable distributions taken from Table 2.

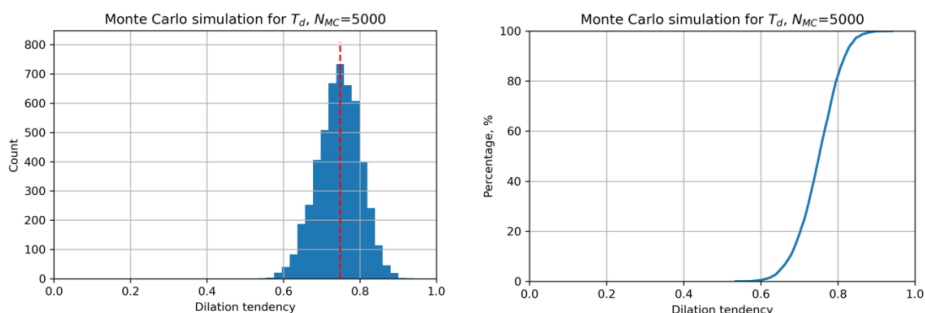


814

815 **Figure A1.** Histograms of input variables used to calculate dilation tendency  $T_d$  for the synthetic distributions  
 816 shown in Table 2.



817 **Figure A2.** Residual plots for linear and quadratic response surfaces for dilation tendency using synthetic  
 818 data. The quadratic fit has a higher value of the adjusted  $R^2$  parameter and is therefore deemed better in this  
 819 case.



820

821 **Figure A3.** Output from Monte Carlo simulation ( $N_{MC}=5,000$ ) of dilation tendency calculated using a quadratic  
822 response surface from synthetic input data. **a.** Histogram of calculated dilation tendency values, in this case  
823 showing a quasi-normal distribution with a mode of  $\sim 0.75$ . **b.** Cumulative distribution function (CDF) of  
824 calculated dilation tendency values, showing the range in values from  $\sim 0.5$  to  $\sim 0.9$ .

825

#### 826 **Code availability**

827 <https://github.com/DaveHealy-github/pfs>

828

#### 829 **Data availability**

830

#### 831 **Author contribution**

832 DH – 80%, SH – 20%. DH originated the study, wrote the code, ran the models. SH contributed seismology  
833 data and expertise, and contributed to the writing of the text.

834

#### 835 **Competing interests**

836 The authors declare that they have no conflicts of interest.

837

#### 838 **Acknowledgements**

839 DH first presented the core ideas in this paper at the Tectonic Studies Group AGM in Cardiff in 2014, and  
840 enjoyed discussions there with Dr Jonathan Turner (RWM Ltd). Thanks to former PhD student Dr Sarah  
841 Weihmann (now at BGR) and co-supervisor Dr Frauke Schaeffer (Wintershall DEA) for discussions about using  
842 oil industry wireline log data for quantifying geomechanical models. GMT (Wessel et al., 2013) was used for  
843 the maps. SciPy (Virtanen et al., 2021), Numpy (Harris et al., 2020), and matplotlib (Hunter, 2007) were used  
844 for the Python pfs code and Allmendinger et al. (2012) for various geomechanical and geometrical algorithms.

845

#### 846 **References**

847 Alcalde, J., Bond, C.E., Johnson, G., Ellis, J.F. and Butler, R.W., 2017. Impact of seismic image quality on fault  
848 interpretation uncertainty. GSA Today.  
849 Allmendinger, R.W., Cardozo, N. and Fisher, D.M., 2011. Structural geology algorithms: Vectors and tensors.  
850 Cambridge University Press.



- 851 Anderson, E.M., 1905. The dynamics of faulting. *Transactions of the Edinburgh Geological Society*, 8(3),  
852 pp.387-402.
- 853 Anthony, R.E., Ringler, A.T., Wilson, D.C. and Wolin, E., 2019. Do low-cost seismographs perform well enough  
854 for your network? An overview of laboratory tests and field observations of the OSOP Raspberry Shake 4D.  
855 *Seismological Research Letters*, 90(1), pp.219-228.
- 856 Ayash, S.C., Dobroskok, A.A., Sorensen, J.A., Wolfe, S.L., Steadman, E.N. and Harju, J.A., 2009. Probabilistic  
857 approach to evaluating seismicity in CO<sub>2</sub> storage risk assessment. *Energy Procedia*, 1(1), pp.2487-2494.
- 858 Baptie, B., 2010. Seismogenesis and state of stress in the UK. *Tectonophysics*, 482(1-4), pp.150-159.
- 859 Barcelona, H., Yagupsky, D., Vigide, N. and Senger, M., 2019. Structural model and slip-dilation tendency  
860 analysis at the Copahue geothermal system: inferences on the reservoir geometry. *Journal of Volcanology  
861 and Geothermal Research*, 375, pp.18-31.
- 862 Batchelor, A.S. and Pine, R.J., 1986, August. The results of in situ stress determinations by seven methods to  
863 depths of 2500 m in the Carnmenellis granite. In *ISRM International Symposium*. OnePetro.
- 864 Beamish, D. and Busby, J., 2016. The Cornubian geothermal province: heat production and flow in SW  
865 England: estimates from boreholes and airborne gamma-ray measurements. *Geothermal Energy*, 4(1), pp.1-  
866 25.
- 867 Becker, A. and Davenport, C.A., 2001. Contemporary in situ stress determinations at three sites in Scotland  
868 and northern England. *Journal of Structural Geology*, 23(2-3), pp.407-419.
- 869 Blenkinsop, T.G., Long, R.E., Kuszniir, N.J. and Smith, M.J., 1986. Seismicity and tectonics in Wales. *Journal of  
870 the Geological Society*, 143(2), pp.327-334.
- 871 Bond, C.E., 2015. Uncertainty in structural interpretation: Lessons to be learnt. *Journal of Structural Geology*,  
872 74, pp.185-200.
- 873 Box, G.E., 1951. Wilson. KB [1951] On the Experimental Attainment of Optimum Conditions. *Journal of the  
874 Royal Statistical Society, Series B (Methodological)*, 13(1), pp.1-45.
- 875 Caine, J.S., Evans, J.P. and Forster, C.B., 1996. Fault zone architecture and permeability structure. *Geology*,  
876 24(11), pp.1025-1028.
- 877 Carvell, J., Blenkinsop, T., Clarke, G. and Tonelli, M., 2014. Scaling, kinematics and evolution of a polymodal  
878 fault system: Hail Creek Mine, NE Australia. *Tectonophysics*, 632, pp.138-150.
- 879 Chang, C., Zoback, M.D. and Khaksar, A., 2006. Empirical relations between rock strength and physical  
880 properties in sedimentary rocks. *Journal of Petroleum Science and Engineering*, 51(3-4), pp.223-237.
- 881 Chiamonte, L., Zoback, M.D., Friedmann, J. and Stamp, V., 2008. Seal integrity and feasibility of CO<sub>2</sub>  
882 sequestration in the Teapot Dome EOR pilot: geomechanical site characterization. *Environmental Geology*,  
883 54(8), pp.1667-1675.
- 884 Clarke, H., Verdon, J.P., Kettleley, T., Baird, A.F. and Kendall, J.M., 2019. Real-time imaging, forecasting, and  
885 management of human-induced seismicity at Preston New Road, Lancashire, England. *Seismological  
886 Research Letters*, 90(5), pp.1902-1915.
- 887 Cochran, E.S., 2018. To catch a quake. *Nature communications*, 9(1), pp.1-4.
- 888 CCC (UK Committee on Climate Change), 2019. Net Zero—Technical Report.
- 889 Cuss, R.J., Rutter, E.H. and Holloway, R.F., 2003. The application of critical state soil mechanics to the  
890 mechanical behaviour of porous sandstones. *International Journal of Rock Mechanics and Mining Sciences*,  
891 40(6), pp.847-862.



- 892 Das, D. and Mallik, J., 2020. Koyna earthquakes: a review of the mechanisms of reservoir-triggered seismicity  
893 and slip tendency analysis of subsurface faults. *Acta Geophysica*, pp.1-16.
- 894 Elsworth, D., Spiers, C.J. and Niemeijer, A.R., 2016. Understanding induced seismicity. *Science*, 354(6318),  
895 pp.1380-1381.
- 896 Farr, G., Sadasivam, S., Watson, I.A., Thomas, H.R. and Tucker, D., 2016. Low enthalpy heat recovery potential  
897 from coal mine discharges in the South Wales Coalfield. *International Journal of Coal Geology*, 164, pp.92-  
898 103.
- 899 Farr, G., Busby, J., Wyatt, L., Crooks, J., Schofield, D.I. and Holden, A., 2021. The temperature of Britain's  
900 coalfields. *Quarterly Journal of Engineering Geology and Hydrogeology*, 54(3).
- 901 Faulkner, D.R., Jackson, C.A.L., Lunn, R.J., Schlische, R.W., Shipton, Z.K., Wibberley, C.A.J. and Withjack, M.O.,  
902 2010. A review of recent developments concerning the structure, mechanics and fluid flow properties of fault  
903 zones. *Journal of Structural Geology*, 32(11), pp.1557-1575.
- 904 Fellgett, M.W., Kingdon, A., Williams, J.D. and Gent, C.M., 2018. Stress magnitudes across UK regions: New  
905 analysis and legacy data across potentially prospective unconventional resource areas. *Marine and  
906 Petroleum Geology*, 97, pp.24-31.
- 907 Fellgett, M.W. and Haslam, R., 2021, April. Fractures in Granite: Results from United Downs Deep Geothermal  
908 well UD-1. In EGU General Assembly Conference Abstracts (pp. EGU21-5593).
- 909 Ferrill, D.A., Winterle, J., Wittmeyer, G., Sims, D., Colton, S., Armstrong, A. and Morris, A.P., 1999. Stressed  
910 rock strains groundwater at Yucca Mountain, Nevada. *GSA Today*, 9(5), pp.1-8.
- 911 Goebel, T.H.W., Rosson, Z., Brodsky, E.E. and Walter, J.I., 2019. Aftershock deficiency of induced earthquake  
912 sequences during rapid mitigation efforts in Oklahoma. *Earth and Planetary Science Letters*, 522, pp.135-143.
- 913 Green, A.S.P., Baria, R., Madge, A. and Jones, R., 1988. Fault-plane analysis of microseismicity induced by  
914 fluid injections into granite. *Geological Society, London, Engineering Geology Special Publications*, 5(1),  
915 pp.415-422.
- 916 Hackston, A. and Rutter, E., 2016. The Mohr–Coulomb criterion for intact rock strength and friction—a re-  
917 evaluation and consideration of failure under polyaxial stresses. *Solid Earth*, 7(2), pp.493-508.
- 918 Hardebeck, J. L., & Shearer, P. M., 2002. A new method for determining first-motion focal  
919 mechanisms. *Bulletin of the Seismological Society of America*, 92(6), 2264-2276.
- 920 Harris, C.R., Millman, K.J., van der Walt, S.J., Gommers, R., Virtanen, P., Cournapeau, D., Wieser, E., Taylor,  
921 J., Berg, S., Smith, N.J. and Kern, R., 2020. Array programming with NumPy. *Nature*, 585(7825), pp.357-362.
- 922 Healy, D., Rizzo, R.E., Cornwell, D.G., Farrell, N.J., Watkins, H., Timms, N.E., Gomez-Rivas, E. and Smith, M.,  
923 2017. FracPaQ: A MATLAB™ toolbox for the quantification of fracture patterns. *Journal of Structural Geology*,  
924 95, pp.1-16.
- 925 Heidbach, O., Rajabi, M., Cui, X., Fuchs, K., Müller, B., Reinecker, J., Reiter, K., Tingay, M., Wenzel, F., Xie, F.  
926 and Ziegler, M.O., 2018. The World Stress Map database release 2016: Crustal stress pattern across scales.  
927 *Tectonophysics*, 744, pp.484-498.
- 928 Hennings, P.H., Lund Snee, J.E., Osmond, J.L., DeShon, H.R., Dommissie, R., Horne, E., Lemons, C. and Zoback,  
929 M.D., 2019. Injection-induced seismicity and fault-slip potential in the Fort Worth Basin, Texas. *Bulletin of  
930 the Seismological Society of America*, 109(5), pp.1615-1634.
- 931 Hicks, S. P., Verdon, J., Baptie, B., Luckett, R., Mildon, Z. K., & Gernon, T., 2019. A shallow earthquake swarm  
932 close to hydrocarbon activities: Discriminating between natural and induced causes for the 2018–2019  
933 Surrey, United Kingdom, earthquake sequence. *Seismological Research Letters*, 90(6), 2095-2110.



- 934 Hicks, S., Goes, S., Whittaker, A. C., & Stafford, P. J., 2021. Multivariate statistical appraisal of regional  
935 susceptibility to induced seismicity: application to the Permian Basin, SW United States. EarthArXiv.  
936 <https://doi.org/10.31223/X5NW3D>
- 937 Hincks, T., Aspinall, W., Cooke, R. and Gernon, T., 2018. Oklahoma's induced seismicity strongly linked to  
938 wastewater injection depth. *Science*, 359(6381), pp.1251-1255.
- 939 Holmgren, J.M. and Werner, M.J., 2021. Raspberry Shake Instruments Provide Initial Ground-Motion  
940 Assessment of the Induced Seismicity at the United Downs Deep Geothermal Power Project in Cornwall,  
941 United Kingdom. *The Seismic Record*, 1(1), pp.27-34.
- 942 Hunter, J.D., 2007. Matplotlib: A 2D graphics environment. *Computing in science & engineering*, 9(03), pp.90-  
943 95.
- 944 IPCC, 2018. *In: Masson-Delmotte, V., Zhai, P., Pörtner, H.O., Roberts, D., Skea, J., Shukla, P.R., Pirani, A.,  
945 Moufouma-Okia, W., Péan, C., Pidcock, R. and Connors, S., 2018. Global warming of 1.5 C. An IPCC Special  
946 Report on the impacts of global warming of, 1, pp.1-9.*
- 947 Jaeger, J.C., Cook, N.G. and Zimmerman, R., 2009. *Fundamentals of rock mechanics*. John Wiley & Sons.
- 948 Jacquey, A.B., Cacace, M., Blöcher, G. and Scheck-Wenderoth, M., 2015. Numerical investigation of  
949 thermoelastic effects on fault slip tendency during injection and production of geothermal fluids. *Energy  
950 Procedia*, 76, pp.311-320.
- 951 Kingdon, A., Fellgett, M.W. and Williams, J.D., 2016. Use of borehole imaging to improve understanding of  
952 the in-situ stress orientation of Central and Northern England and its implications for unconventional  
953 hydrocarbon resources. *Marine and Petroleum Geology*, 73, pp.1-20.
- 954 Ledingham, P., Cotton, L. and Law, R., 2019, February. The united downs deep geothermal power project. In  
955 *Proceedings of the 44th Workshop on Geothermal Reservoir Engineering*, Stanford University, Stanford, CA,  
956 USA (pp. 11-13).
- 957 Li, X., Main, I. and Jupe, A., 2018. Induced seismicity at the UK 'hot dry rock' test site for geothermal energy  
958 production. *Geophysical Journal International*, 214(1), pp.331-344.
- 959 Lisle, R.J. and Srivastava, D.C., 2004. Test of the frictional reactivation theory for faults and validity of fault-  
960 slip analysis. *Geology*, 32(7), pp.569-572.
- 961 McLennan, D., Noble, S., Noble, M., Plunkett, E., Wright, G. and Gutacker, N., 2019. *The English indices of  
962 deprivation 2019: Technical report*.
- 963 Miocic, J.M., Johnson, G. and Bond, C.E., 2019. Uncertainty in fault seal parameters: implications for CO<sub>2</sub>  
964 column height retention and storage capacity in geological CO<sub>2</sub> storage projects. *Solid earth*, 10(3), pp.951-  
965 967.
- 966 Moeck, I., Kwiatek, G. and Zimmermann, G., 2009. Slip tendency analysis, fault reactivation potential and  
967 induced seismicity in a deep geothermal reservoir. *Journal of Structural Geology*, 31(10), pp.1174-1182.
- 968 Moos, D., Peska, P., Finkbeiner, T. and Zoback, M., 2003. Comprehensive wellbore stability analysis utilizing  
969 quantitative risk assessment. *Journal of Petroleum Science and Engineering*, 38(3-4), pp.97-109.
- 970 Morris, A., Ferrill, D.A. and Henderson, D.B., 1996. Slip-tendency analysis and fault reactivation. *Geology*,  
971 24(3), pp.275-278.
- 972 Musson, R.M., 1996. The seismicity of the British Isles. *Annals of Geophysics*, 39(3).
- 973 Myers, R.H., Montgomery, D.C. and Anderson-Cook, C.M., 2016. *Response surface methodology: process and  
974 product optimization using designed experiments*. John Wiley & Sons.
- 975 Nolan, L., 2016, July. The Welsh Index of Multiple Deprivation. In *Presentation for the GSS Methodology  
976 Conference (Vol. 6)*.



- 977 Pine, R.J. and Batchelor, A.S., 1984, October. Downward migration of shearing in jointed rock during hydraulic  
978 injections. In International Journal of Rock Mechanics and Mining Sciences & Geomechanics Abstracts (Vol.  
979 21, No. 5, pp. 249-263). Pergamon.
- 980 Raymond, E., 2001. The Cathedral & the Bazaar, Revised Edition. O'Reilly.
- 981 Roberts, J. J., Bond, C. E., & Shipton, Z. K., 2021. Fracking bad language—hydraulic fracturing and earthquake  
982 risks. *Geoscience Communication*, 4(2), 303-327.
- 983 Rohmer, J. and Bouc, O., 2010. A response surface methodology to address uncertainties in cap rock failure  
984 assessment for CO<sub>2</sub> geological storage in deep aquifers. *International Journal of Greenhouse Gas Control*,  
985 4(2), pp.198-208.
- 986 Rutter, E.H. and Hadzadeh, J., 1991. On the influence of porosity on the low-temperature brittle—ductile  
987 transition in siliciclastic rocks. *Journal of Structural Geology*, 13(5), pp.609-614.
- 988 Sanchez, C., Saldi, G., Mitchell, T., Iacoviello, F., Meredith, P., Jones, A., Oelkers, E., and Striolo, A., 2020. The  
989 role of fluid chemistry on permeability and fault strength evolution in granite, EGU General Assembly 2020,  
990 Online, 4–8 May 2020, EGU2020-21850, <https://doi.org/10.5194/egusphere-egu2020-21850>
- 991 Sanchez-Roa, C., Saldi, G.D., Mitchell, T.M., Iacoviello, F., Bailey, J., Shearing, P.R., Oelkers, E.H., Meredith,  
992 P.G., Jones, A.P. and Striolo, A., 2021. The role of fluid chemistry on permeability evolution in granite:  
993 Applications to natural and anthropogenic systems. *Earth and Planetary Science Letters*, 553, p.116641.
- 994 Stephenson, M.H., Ringrose, P., Geiger, S., Bridden, M. and Schofield, D., 2019. Geoscience and  
995 decarbonization: current status and future directions. *Petroleum Geoscience*, 25(4), pp.501-508.
- 996 Stirling, M.W., Wesnousky, S.G. and Shimazaki, K., 1996. Fault trace complexity, cumulative slip, and the  
997 shape of the magnitude-frequency distribution for strike-slip faults: A global survey. *Geophysical Journal  
998 International*, 124(3), pp.833-868.
- 999 Streit, J.E. and Hillis, R.R., 2004. Estimating fault stability and sustainable fluid pressures for underground  
1000 storage of CO<sub>2</sub> in porous rock. *Energy*, 29(9-10), pp.1445-1456.
- 1001 Townend, J. and Zoback, M.D., 2000. How faulting keeps the crust strong. *Geology*, 28(5), pp.399-402.
- 1002 Verdon, J.P. and Budge, J., 2018. Examining the capability of statistical models to mitigate induced seismicity  
1003 during hydraulic fracturing of shale gas reservoirs. *Bulletin of the Seismological Society of America*, 108(2),  
1004 pp.690-701.
- 1005 Virtanen, P., Gommers, R., Oliphant, T.E., Haberland, M., Reddy, T., Cournapeau, D., Burovski, E., Peterson,  
1006 P., Weckesser, W., Bright, J. and Van Der Walt, S.J., 2020. SciPy 1.0: fundamental algorithms for scientific  
1007 computing in Python. *Nature methods*, 17(3), pp.261-272.
- 1008 Walker, A., Baptie, B. and Ottemoller, L., 2003. UK earthquake monitoring 2002/2003.
- 1009 Walsh III, F.R. and Zoback, M.D., 2016. Probabilistic assessment of potential fault slip related to injection-  
1010 induced earthquakes: Application to north-central Oklahoma, USA. *Geology*, 44(12), pp.991-994.
- 1011 Walsh, J.J., Childs, C., Meyer, V., Manzocchi, T., Imber, J., Nicol, A., Tuckwell, G., Bailey, W.R., Bonson, C.G.,  
1012 Watterson, J. and Nell, P.A., 2001. Geometric controls on the evolution of normal fault systems. *Geological  
1013 Society, London, Special Publications*, 186(1), pp.157-170.
- 1014 Wang, Q., Ru, Z., Zhao, R., Yu, C., Liu, Y. and Deng, S., 2020. A study on permeability along strike slip faults in  
1015 Shunbei reservoir of Tarim Basin, China. *Energy Sources, Part A: Recovery, Utilization, and Environmental  
1016 Effects*, pp.1-17.
- 1017 Wesnousky, S.G., 1988. Seismological and structural evolution of strike-slip faults. *Nature*, 335(6188), pp.340-  
1018 343.



- 1019 Wessel, P., Smith, W.H., Scharroo, R., Luis, J. and Wobbe, F., 2013. Generic mapping tools: improved version  
1020 released. *Eos, Transactions American Geophysical Union*, 94(45), pp.409-410.
- 1021 Wibberley, C.A., Yielding, G. and Di Toro, G., 2008. Recent advances in the understanding of fault zone  
1022 internal structure: a review. Geological Society, London, Special Publications, 299(1), pp.5-33.
- 1023 Williams, J.D., Fellgett, M.W. and Quinn, M.F., 2016. Carbon dioxide storage in the Captain Sandstone aquifer:  
1024 determination of in situ stresses and fault-stability analysis. *Petroleum Geoscience*, 22(3), pp.211-222.
- 1025 Williams, J.D.O., Gent, C.M.A., Fellgett, M.W. and Gamboa, D., 2018. Impact of in situ stress and fault  
1026 reactivation on seal integrity in the East Irish Sea Basin, UK. *Marine and Petroleum Geology*, 92, pp.685-696.
- 1027 Zhao, J., 1987. Experimental studies of the hydro-thermo-mechanical behaviour of joints in granite. Unpubl.  
1028 PhD thesis, Imperial College, London, UK.
- 1029